

Winter Dynamics in an Epishelf Lake: Quantitative Mixing Estimates and Ice Shelf Basal Channel Considerations

J r mie Bonneau¹, Bernard Laval¹, Derek R Mueller², Alexander LeBaron Forrest³, Andrew MacWhorter Friedrichs⁴, and Andrew K Hamilton⁵

¹University of British Columbia

²Carleton University

³University of California - Davis

⁴UC Davis

⁵University of Alberta

November 22, 2022

Abstract

Milne Ice Shelf is located at the mouth of Milne Fiord (82.6 $^{\circ}$ N, 81.0 $^{\circ}$ W), on Ellesmere Island, Nunavut. This floating ice feature is attached to both sides of the fjord. During the melt season, the ice shelf acts as a dam preventing surface runoff from flowing freely to the ocean. This results in a permanent layer of freshwater that “floats” on top of the seawater of the fjord, commonly known as an epishelf lake. The winter data from a mooring installed in Milne Fiord epishelf lake (2011-2019) is analysed in the framework of a one-dimensional model in order to 1) study mixing in the upper water column and 2) infer the characteristics of a basal channel in the ice shelf. The results show that vertical mixing rates are higher in the epishelf lake than in the seawater below. Estimation of the Richardson number using a geostrophic balance approach reveals that enhanced mixing in the epishelf lake is associated with horizontal temperature gradients. Moreover, the analysis suggests that the epishelf lake water reaching the ocean travels through a single basal channel in the ice shelf. The model did not detect significant variation in outflow characteristics over the eight years of study, implying that the area of the basal channel is in ice mass balance.

1 **Winter Dynamics in an Epishelf Lake: Quantitative**
2 **Mixing Estimates and Ice Shelf Basal Channel**
3 **Considerations**

4 **J. Bonneau¹, B. E. Laval¹, D. Mueller², A. K. Hamilton³, A. M. Friedrichs^{4,5},**
5 **A. L. Forrest^{4,5}**

6 ¹Department of Civil Engineering, University of British Columbia, Vancouver, BC, Canada

7 ²Department of Geography and Environmental Studies, Carleton University, Ottawa, ON, Canada

8 ³Earth and Atmospheric Sciences, University of Alberta, Edmonton, AB, Canada

9 ⁴Civil and Environmental Engineering, University of California Davis, CA, USA.

10 ⁵Tahoe Environmental Research Center, University of California Davis, CA, USA.

11 **Key Points:**

- 12 • A one-dimensional model is used to analyse eight years of winter mooring data
13 of the upper water column in an perennially ice-covered fjord.
14 • Mixing is more pronounced in the isolated freshwater layer (epishelf lake) than in
15 the seawater below.
16 • Epishelf lake water exits the fjord through a basal channel under the ice shelf. The
17 channel is apparently not evolving rapidly.

Abstract

Milne Ice Shelf is located at the mouth of Milne Fiord (82.6°N, 81.0°W), on Ellesmere Island, Nunavut. This floating ice feature is attached to both sides of the fjord. During the melt season, the ice shelf acts as a dam preventing surface runoff from flowing freely to the ocean. This results in a permanent layer of freshwater that “floats” on top of the seawater of the fjord, commonly known as an epishelf lake. The winter data from a mooring installed in Milne Fiord epishelf lake (2011-2019) is analysed in the framework of a one-dimensional model in order to 1) study mixing in the upper water column and 2) infer the characteristics of a basal channel in the ice shelf. The results show that vertical mixing rates are higher in the epishelf lake than in the seawater below. Estimation of the Richardson number using a geostrophic balance approach reveals that enhanced mixing in the epishelf lake is associated with horizontal temperature gradients. Moreover, the analysis suggests that the epishelf lake water reaching the ocean travels through a single basal channel in the ice shelf. The model did not detect significant variation in outflow characteristics over the eight years of study, implying that the area of the basal channel is in ice mass balance.

Plain Language Summary

An ice shelf is a thick floating sheet of ice attached to the land. At the mouth of Milne Fiord, on the northern coast of Ellesmere Island, is Milne Ice Shelf. Milne Ice Shelf is attached to the land on both sides of the fjord and acts like a dam preventing fresh meltwater from the watershed from directly flowing out to the ocean. This creates a layer of freshwater floating on top of the seawater, called an epishelf lake. In this study, we use field observations and a numerical model to conclude that there is more mixing in the epishelf lake than in the seawater below. Moreover, we suggest that most of the water flowing out of the epishelf lake follows a channel under the ice shelf and that this channel has not evolved significantly from 2011 to 2019.

1 Introduction

In the Canadian High Arctic, all major glaciers north of the 74th parallel are losing mass as a result of atmospheric warming (Mortimer et al., 2018). Climate-related changes are unmistakable on the northern coast of Ellesmere Island where the ice shelf extent has considerably decreased over the last century (Mueller et al., 2017). In this region, where historically there was an ice shelf at the mouth of every fjord (Vincent et al., 2001), the continuous fracture and break up of ice shelves left only one relatively intact in Milne Fiord. portions of the Milne Ice Shelf are attached to land on both sides of the fjord. Therefore, it acts like a dam, preventing freshwater from surface runoff from dispersing freely into the ocean. This perennial layer of freshwater overlying Arctic seawater landward of the ice shelf is referred to as an epishelf lake. Since Milne Ice Shelf (MIS) is the only ice shelf in Canada that had not broken up, Milne Fiord epishelf lake (MEL) is the last epishelf lake along its coast. Several other epishelf lakes can be found in Antarctica (Laybourn-Parry & Wadham, 2014; Gibson & Andersen, 2002) and one in Greenland (Bennike & Weidick, 2001). In late July 2020, ~43% of MIS calved along its seaward front.

The dynamics of the Milne epishelf lake and Milne Ice Shelf are closely linked. It is thought that the epishelf lake outflows through a basal channel under the ice shelf. Therefore, it is hypothesized that the morphology of the channel controls the thickness of the epishelf lake (Hamilton et al., 2017). The basal channel under Milne Ice Shelf is analogous to those found beneath Petermann Glacier in Greenland (Rignot & Steffen, 2008; Washam et al., 2019) or Pine Island Glacier Ice Shelf (Stanton et al., 2013; Dutrieux et al., 2013) in Antarctica. These basal channels have attracted attention in recent years as meltwater concentrates in these features (Millgate et al., 2013; Gladish et al., 2012)

and increases local melt rates (Stanton et al., 2013; Dutrieux et al., 2013; Alley et al., 2016). It is generally thought that the localized strong melting within channels leads to faster breakup as a result of weakening of the overall structure (Dow et al., 2018; Gourmelon et al., 2017; Rignot & Steffen, 2008). However, numerical modeling has shown that these channels could potentially reduce the overall melting of ice shelf, resulting in a stabilization effect (Gladish et al., 2012).

From an oceanographic perspective, the physical structure of the upper water column in Milne Fiord is well known during summer (Hamilton et al., 2017), but less so during winter. Because the fjord is perennially ice-covered, no wind-induced circulation or mixing occurs. Moreover, the tidal amplitudes are very small (~ 10 cm). However, other mechanisms can modify the water column in ice-covered fjords. Sciascia et al. (2013) found that even during the winter, meltwater plumes influenced the circulation in Sermilik Fjord, Greenland. Also in Sermilik, R. H. Jackson et al. (2014) and Straneo et al. (2010) showed that water properties changed in response to along-shore wind episodes creating downwelling events. The Earth’s rotation can also alter the currents in a fjord when it is sufficiently wide (i.e. larger than the Rossby radius) (Straneo & Cenedese, 2015; R. H. Jackson et al., 2018), changing the circulation from a two dimensional to a three dimensional pattern.

Furthermore, due to the presence of the ice shelf, the upper water column in Milne Fiord has similarities with ice-covered lakes, where the influence of the Earth’s rotation on the circulation pattern has also been reported (e.g. Bengtsson, 1996; Rizk et al., 2014; Huttula et al., 2010; Forrest et al., 2013; Steel et al., 2015). In some cases, heat fluxes at the boundaries combine with Coriolis force to generate circulation features in geostrophic or cyclogeostrophic balance. These boundary heat fluxes can be the result of sediment (Rizk et al., 2014), inflows and solar heating of moat water (Kirillin et al., 2015) or melting of ice along an ice wall (Steel et al., 2015).

Since there is a strong interconnection between the ice shelf, the epishelf lake and the glacier, quantitative information about circulation and mixing processes is important to better understand the outflow in the channel and the amount of surface runoff. Furthermore, this information would also improve insights on the fate of the ice structures in the fjord (e.g. ice shelf, glacier and lake ice). Finally, in addition to other epishelf lakes in Antarctica, physical processes in MEL can be similar to those in ice-covered lakes, where external forcing is limited, especially when snow cover significantly reduces solar radiation reaching the water. Since it is perennially ice-covered, Milne epishelf lake studies also provide an understanding of ice-covered lake processes.

This study has two main objectives. The first is to quantify vertical mixing occurring in the epishelf lake and associate it with a forcing mechanisms. The second is to confirm that the basal channel is the main outflow path for the epishelf lake and to infer the evolution of its morphology. In order to do this, a one-dimensional model was calibrated with the mooring data (July 2011 to July 2019) to estimate the mixing in the top of the water column and the discharge through the channel in winter.

2 Geophysical Setting and Study Area Background

2.1 Milne Fiord

Figure 1 is a satellite image of Milne Fiord showing the downstream part of Milne Glacier (MG), the glacier tongue (MGT), the epishelf lake (MEL) and the ice shelf (MIS). The main part of MEL is between MIS and MGT, although there is an arm on each side of MGT. Milne Fiord is 40 km long from the glacier grounding line to the outer edge of the ice shelf (prior to the 2020 calving event). Its width is 6 km from the glacier grounding line to the epishelf lake and then becomes wider downfjord. The bathymetry of the fjord, inferred from CTD casts and depth soundings (Hamilton et al., 2017) exhibits a U-shape profile with a maximum depth of 436 m. A 220 m deep sill is inferred to exist just downfjord of the epishelf lake. The maximum fjord depth below the epishelf lake

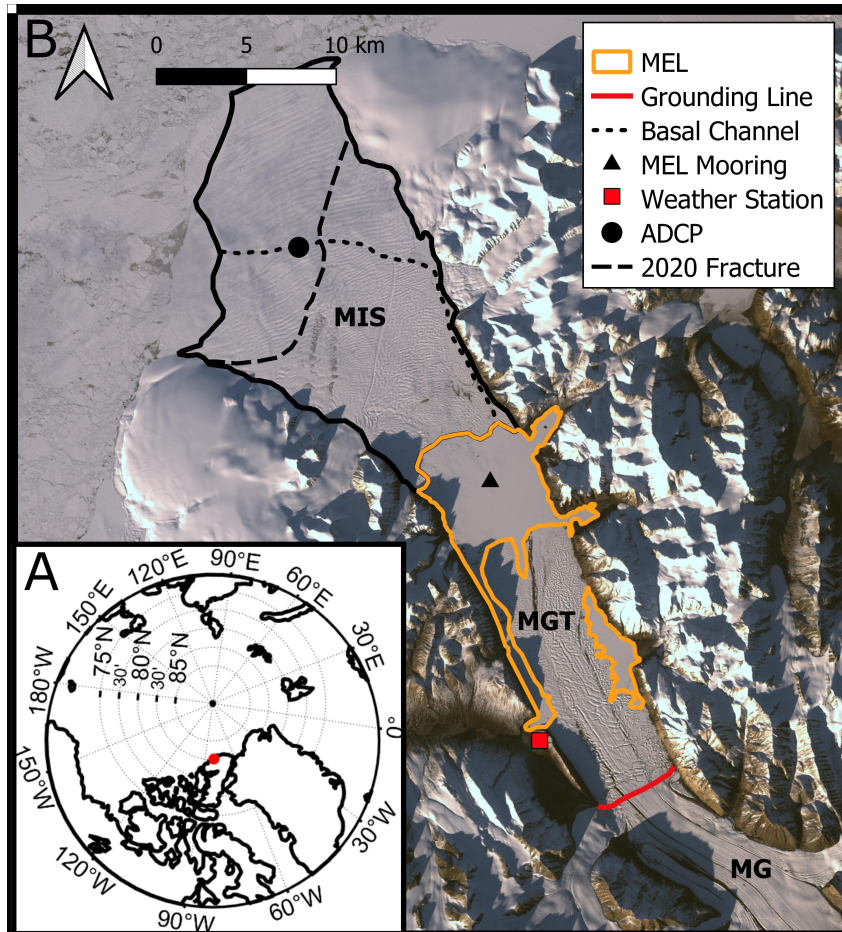


Figure 1. A) Location of Milne Fiord (82.6°N, 81.0°W). B) Landsat 8 image of Milne Fiord taken in September 2018. MEL: Milne Epishelf Lake, MIS: Milne Ice Shelf, MGT: Milne Glacier Tongue, MG: Milne Glacier. MIS calved along the long dash line in July 2020.

is approximately 430 m and the depth near the grounding line of Milne Glacier is 150 m. Tides in Milne Fiord are semidiurnal with an amplitude of ~ 10 cm. Tidal baroclinicity was observed in current measurements but was too low to produce shear mixing (Hamilton et al., 2017). The average annual air temperature at sea level is -19°C , with the number of positive degree days (a proxy for surface melting) between 100 and 300 from June 1st to September 1st (Hamilton, 2016). At this high latitude, there is no direct solar radiation from mid-October to the beginning of March. Oceanographic measurements on the Ellesmere Island shelf are extremely sparse. It is however acknowledge that it is a relatively quiet zone with weak currents (J. M. Jackson et al., 2014; Aksenov et al., 2011).

2.2 Milne Glacier and Milne Ice Shelf

MG is over 50 km long and is 4 to 5 km wide. It has a thickness of approximately 150 m at the grounding line (Hamilton, 2016). Downfjord from the grounding line, MGT extends 15 km. The thickness of the MGT decreases rapidly and the ice thickness is less than 10 m at its margins. It broke away from the glacier in 2009 but has not moved significantly since.

Before July 2020, MIS occupied 200 km^2 at the mouth of Milne Fiord. The estimated mean ice thickness was 47 m with a maximum and a minimum around 94 m and 8 m, respectively (Hamilton, 2016; Mortimer et al., 2012). The thinnest area was along a basal channel that runs westward from the east shore (Hamilton et al., 2017; Mortimer et al., 2012; Rajewicz, 2017) (Figure 1). Figure 1 shows the line of fracture where MIS calved at the end of July 2020. Approximately 86 km^2 broke away, including some area where the ice was the thickest (over 80 m). The break up happened during open ocean conditions offshore.

2.3 Milne Fiord Epishelf Lake

From a physical perspective, the most striking feature of the MEL is the extremely sharp salinity interface between the freshwater and the ocean below. The depth of the halocline, taken as the depth of maximum density stratification, is used as a definition of the depth of the epishelf lake (Hamilton et al., 2017).

MEL experiences an annual cycle of deepening and shoaling. Summer is here defined as the period between the first and last day with a least one hour of air temperature over 0°C . Winter is defined as the period between two summers. During the summer, when snow and ice are melting, water from surface runoff flows into the lake deepening the freshwater layer (Figure 2A). Meanwhile, water deeper than the minimum draft of the ice shelf flows to the ocean. When summer is over, surface runoff stops and the lake slowly shoals until summer (Figure 2B). It is thought that the flow of epishelf lake water to the ocean is exclusively along the ice shelf basal channel and is hydraulically controlled by its dimensions (Hamilton et al., 2017; Rajewicz, 2017). This study tests this hypothesis by modeling the outflow during the winter period. Using satellite imagery, it is estimated that MEL covers 71.2 km^2 . As a result of short summers, cold long winters and a freshwater cap, the lake is permanently ice-covered. The minimum ice thickness observed was 0.65 m in July 2010 (Hamilton, 2016) and a maximum of 3.19 m was observed in May 1983 (Jeffries, 1985).

3 Data and Methods

3.1 Field Observations

A mooring tethered to the ice was deployed in the center of MEL in May 2011 and has been recording since then. The data from the original deployment to July 2019 are analyzed here. The only time gaps are during fieldwork when the mooring was serviced. Over the years, the mooring configuration changed substantially and different instruments

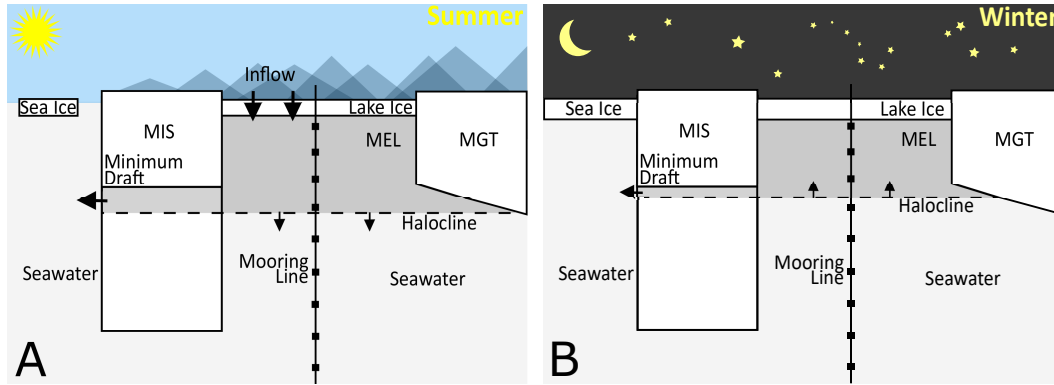


Figure 2. Schematic of Milne Fiord including Milne Ice Shelf (MIS), Milne Epishelf Lake (MEL) and Milne Glacier Tongue (MGT). A) During the melt season (summer) (\sim June 1st to \sim September 1st), meltwater inflow drives the deepening of MEL. B) During the remainder of the year, the thickness of MEL decreases slowly toward the minimum draft of the MIS.

168 have been used. Since the focus here is on annual and interannual variations, data from
 169 all the mooring instruments were averaged daily for the following analysis. The accu-
 170 racy of the moored instruments was superior to $\pm 0.01^\circ\text{C}$ and 0.05 mS cm^{-1} (drift included).
 171 When pressure data was available (6 out of 8 years), instrument depth was corrected for
 172 shifts in elevation due to ice formation/melting on the lake (0-0.2 m). All temperature
 173 and salinity data in this study were converted to the TEOS-10 standard as conservative
 174 temperature, Θ [$^\circ\text{C}$] and absolute salinity, S_A [g kg^{-1}] using the GSW oceanographic tool-
 175 box (McDougall & Barker, 2011).

176 Water profiles were taken every summer in MEL. Instruments used for profiling were
 177 an Idronaut Ocean304plus (2015-2016) and an RBR XR-620 (2011-2014, 2017-2019). The
 178 accuracy of these instruments is $\pm 0.002^\circ\text{C}$, $\pm 0.003\text{ mS cm}^{-1}$ and $\pm 0.37\text{ dbar}$, with a drift
 179 of $\pm 0.002^\circ\text{C a}^{-1}$, $\pm 0.012\text{ mS cm}^{-1}\text{ a}^{-1}$, and $\pm 0.7\text{ dbar a}^{-1}$. Calibration was done every
 180 other year and a crosscheck with other CTD instruments was also performed. Profiles
 181 were taken at recovery and deployment of the mooring to crosscheck the mooring instru-
 182 ments and to resolve water properties between them.

183 A weather station installed next to a small bay in Purple Valley (Figure 1) has been
 184 recording hourly data continuously since 2009 (data courtesy: Luke Copland). Data avail-
 185 able is temperature, wind (speed and direction), relative humidity, atmospheric pressure
 186 and solar radiation. A weather station was also installed on the ice shelf from July 2016
 187 to July 2018. Even though the Purple Valley station is sheltered compared to the ice shelf
 188 station, decomposed N-E-S-W winds at $\sim 2\text{ m}$ show similar direction and speed.

189 An acoustic doppler current profiler (ADCP) moored near the apex of the ice shelf
 190 basal channel (Figure 1) recorded from July 2017 to July 2019. The instrument (Tele-
 191 dyne Workhorse 1200kHz) recorded hourly current measurements using 0.2 m (2017-2018)
 192 and 0.25 m (2018-2019) vertical bins. Using the July 2016 channel morphology data from
 193 Rajewicz (2017) and the approximated 71.2 km^2 lake area (Hamilton et al., 2017), the
 194 data from the ADCP and the model can be compared in order to evaluate the model out-
 195 flow over the 2016-2017 and 2017-2018 winter deployments.

196 3.2 Model Formulation

197 A one-dimensional model (Figure 3) was used to analyze the mooring data during
 198 the winter. It is emphasized here that the model was used as a diagnostic tool to exam-
 199 ine mixing and the outflow, not as a prognostic one. It was designed to analyze all of
 200 the available winter data from the mooring in a simplified context with a small number

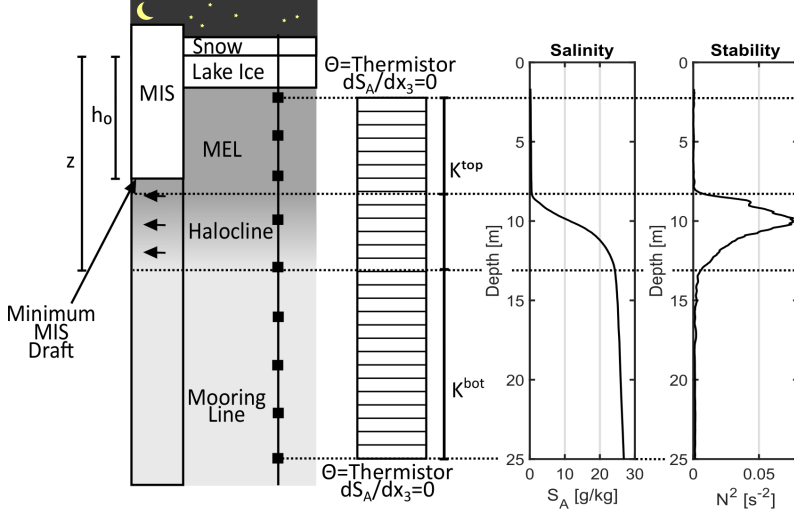


Figure 3. Schematic of the one-dimensional model. Typical absolute salinity and stability profiles are on the right. The data from the uppermost thermistor and the 25 m thermistor are used as boundary conditions for temperature and no-flux boundary conditions are used for salinity. Mixing coefficients of the top freshwater layer (K^{top}) and the bottom seawater layer (K^{bot}) are parameters of the model; only molecular mixing is considered in the halocline layer. The outflow layer is between the minimum draft of the ice shelf (h_0) and the bottom of the halocline layer (z). The top and bottom dashed lines show the top and bottom boundaries of the model. The two middle dashed lines are the top and bottom of the halocline layer (molecular diffusivity only).

201 of free parameters. The model estimates the vertical mixing in the upper water column
 202 and the outflow through the basal channel. In order to do this, the mooring data was
 203 employed to determine the parameters of the model using an iterative method.

204 To model the transport of heat and salt, the Reynolds-averaged transport equation
 205 for scalar properties was used (Kundu et al., 2012):

$$\frac{\partial \bar{\varphi}}{\partial t} + \bar{u}_j \frac{\partial \bar{\varphi}}{\partial x_j} + \frac{\partial(\overline{u'_j \varphi'})}{\partial x_j} = K_m \frac{\partial^2 \bar{\varphi}}{\partial x_j^2} \quad (1)$$

206 Where $\bar{\varphi}$ is a Reynolds-averaged scalar (e.g. conservative temperature or absolute salin-
 207 ity), \bar{u}_j is the Reynolds-averaged velocity vector and K_m is the molecular diffusivity.
 208 t is the time and x is the dimension ($[x_1 \ x_2 \ x_3] = [x \ y \ z]$, x_3 being in the vertical di-
 209 rection). The following simplifying assumptions were made:

- 210 • The average vertical velocity \bar{u}_3 is nil ($\bar{u}_3 = 0$)
- 211 • The horizontal gradients are negligible ($\bar{u}_1 \frac{\partial \bar{\varphi}}{\partial x_1} \approx \bar{u}_2 \frac{\partial \bar{\varphi}}{\partial x_2} \approx \frac{\partial^2 \bar{\varphi}}{\partial x_1^2} \approx \frac{\partial^2 \bar{\varphi}}{\partial x_2^2} \approx \frac{\partial^2 \overline{u'_1 \varphi'}}{\partial x_1^2} \approx$
 212 $\frac{\partial^2 \overline{u'_2 \varphi'}}{\partial x_2^2} \approx 0$)
- 213 • Eddy diffusivity can be used to estimate turbulence ($\overline{u'_3 \varphi'} \approx -K_t \frac{\partial \bar{\varphi}}{\partial x_3}$), with K_t
 214 representing a turbulent eddy diffusivity

215 This leads to:

$$\frac{\partial \bar{\varphi}}{\partial t} = K \frac{\partial^2 \bar{\varphi}}{\partial x_3^2} \quad (2)$$

216 where K is the combined diffusivity ($K = K_t + K_m$), here referred to as the mixing
217 coefficient.

218 In order to take into account the outflow of the epishelf lake (Figure 3), the basal
219 channel was simplified as a rectangular weir (Figure 4), which allowed the outflow to be
220 described. The model works to estimate four different parameters: two mixing coefficients
221 (K^{top} , K^{bot} , see below) for every day and two annual outflow parameters ($C_e b$, h_0 , see
222 below). To find the value of these parameters, these quantities were constrained to a num-
223 ber of possible values and then an iterative method was employed to find the best fit-
224 ting coefficients using the daily averaged mooring data as the evaluation data set. The
225 model was solved on a 10 cm by 30 minute grid using a Crank-Nicolson finite difference
226 scheme. Grid space and time independence was verified by using different mesh sizes.

227 **3.2.1 Boundary conditions**

228 For temperature, the daily averaged data from the uppermost unfrozen thermis-
229 tor and the thermistor at 25 m depth were used as Dirichlet boundary conditions at the
230 top and bottom nodes. For salinity, a no-flux ($\partial \overline{S_A} / \partial z = 0$) boundary condition was
231 used. Since mixing is very limited (as will be shown in the results section), no salt flux
232 at 25 m is a reasonable assumption even though gradients do exist at that depth. This
233 is especially true since the focus here is on the epishelf lake.

234 **3.2.2 Initial conditions**

235 The model was reset at the beginning of every winter with new initial conditions.
236 Each run was started when the water temperature in the lake stopped increasing. For
237 temperature, initial conditions were given by a linear interpolation between the moor-
238 ing instruments. Initial salinity conditions were obtained by using the last CTD cast taken
239 during the field season and fitting this profile to the mooring salinity data by shifting
240 it vertically to get the best fit (minimum RMSE). CTD profiles in July, August and May
241 support this method. Each run was stopped at the first day with positive air temper-
242 ature to ensure no changes in water properties or mixing from surface meltwater inflow.

243 **3.2.3 Mixing**

244 In order to account for mixing, the water column was divided into three layers (fresh-
245 water, halocline and seawater), each with different mixing coefficients (Figure 3). The
246 layer boundaries were defined as the points where the squared Brunt-Visl frequency equaled
247 10^{-2} s^{-2} . This demarcation is supported by the minimum Richardson number ($Ri = N^2 / (\frac{\partial u}{\partial z})^2$)
248 found in the water profile. An observed velocity gradient around 0.01 s^{-1} from Hamilton
249 (2016) and induction current meter measurements (not shown) in combination with per-
250 petual high stratification ($>10^{-2} \text{ s}^{-2}$) made it possible to rule-out turbulent mixing in the
251 halocline. However, within the top freshwater and bottom seawater layers, CTD mea-
252 surements indicate stratification is not strong enough to preclude turbulent mixing. The
253 threshold of 10^{-2} s^{-2} was arbitrarily chosen as it delineates the region of high salinity gra-
254 dient with good precision in all CTD profiles (Figure 3). To summarize:

- 255 • The top layer, from the top boundary to $N^2 = 10^{-2} \text{ s}^{-2}$ had mixing coefficients for
256 heat (K_{Θ}^{top}) and salt (K_{SA}^{top}).
- 257 • The halocline layer, where $N^2 > 10^{-2} \text{ s}^{-2}$, only had molecular diffusion.
- 258 • The bottom layer, from $N^2 = 10^{-2} \text{ s}^{-2}$ to the bottom boundary, had mixing co-
259 efficients for heat (K_{Θ}^{bot}) and salt (K_{SA}^{bot}).

260 Values of $1.4 \times 10^{-7} \text{ m}^2 \text{ s}^{-1}$ and $1.4 \times 10^{-9} \text{ m}^2 \text{ s}^{-1}$ were employed for molecular diffusivities
261 of heat and salt, respectively (P. R. Jackson & Rehmann, 2014). Possible K_{Θ} coefficients
262 were: [1.4, 2, 4, 8, 16, 32, 64, 128, 256, 512, 1024] $\times 10^{-7} \text{ m}^2 \text{ s}^{-1}$. The power of two incre-

263 ment was chosen to reasonably cover orders of magnitude from 10^{-7} to 10^{-4} for K_{Θ} while
 264 keeping the required computational power reasonably low (typical laptop). The upper
 265 limit of $1024 \times 10^{-7} \text{ m}^2 \text{ s}^{-1}$ was chosen as K_{Θ} only very rarely reaches this value (as will
 266 be shown in the presented results).

267 As first pointed out by Turner (1968), when turbulence is weak, the mixing of heat
 268 and salt is not the same (i.e. the turbulent Lewis number ($Le = \frac{K_{t,\Theta}}{K_{t,SA}}$) is not one). Dif-
 269 ferential diffusion ($Le \neq 1$) has been observed in the ocean and demonstrated in labora-
 270 tory and numerical experiments (Gargett, 2003). Because Milne Fiord is a quiet envi-
 271 ronment, it is important to take into account differential diffusion in order to model the
 272 water column properly. To account for this phenomenon, the parameterization of P. R. Jack-
 273 son and Rehmann (2014) was applied to link K_{Θ}^{top} to K_{SA}^{top} and K_{Θ}^{bot} to K_{SA}^{bot} and reduce
 274 the number of unknowns. Using the ratio determined by these authors, possible K_{SA}
 275 coefficients were: $[0.0014, 0.002, 0.004, 1.5, 4.3, 12, 33, 81, 191, 425, 915] \times 10^{-7} \text{ m}^2 \text{ s}^{-1}$.

276 3.2.4 Outflow

277 Assuming most of the water outflow is through the basal channel in the ice shelf
 278 and that it can be simplified as a rectangular channel (Hamilton et al., 2017), the out-
 279 flow was modelled based on an inverse rectangular weir equation (Kindsvater & Carter,
 280 1959) (Figure 4):

$$\frac{d(z - h_0)}{dt} = \frac{2}{3A_{lake}} \sqrt{2g'} C_e b (z - h_0)^{2/3} \quad (3)$$

281 Where h_0 is the depth of the minimum draft of the ice shelf, C_e is a friction coefficient,
 282 b is the width of the rectangular channel, z is the depth at the bottom of the outflow layer
 283 and A_{lake} is the area of the lake ($\sim 71.2 \times 10^3 \text{ m}^2$). g' is the reduced gravity ($\frac{g\Delta\rho}{\rho} \approx 0.25$
 284 m s^{-2}), where g is the gravitational acceleration, $\Delta\rho$ is the density difference between the
 285 freshwater and the seawater (25 kg m^{-3}) and ρ is a reference density (1000 kg m^{-3}). $C_e b$
 286 and h_0 are two unknown parameters that were assumed constant for the duration of each
 287 winter. $\frac{d(z-h_0)}{dt}$ was computed every day and the amount of water flowing out to the ocean
 288 was modeled by shrinking the outflow layer (i.e. $z-h_0$ was reduced). This assumes that
 289 the outflow velocity is the same everywhere in the outflow layer. The above simplifica-
 290 tions were derived from current measurements and ice penetrating radar measurements
 291 over the channel (Rajewicz, 2017). In order to compensate for the outflow, water was
 292 added at the bottom of the model using the properties of the bottom node. Using equa-
 293 tion 3, possible values for h_0 ranged from 3 to 10 m. The possible values for $C_e b$ ranged
 294 from 2 to 10 m, which gives a minimum channel width from 2.5 to 18 m using common
 295 rectangular weir coefficients (0.55 to 0.8) (Hamilton et al., 2017).

296 3.3 Model Fitting

297 In order to find the optimal model parameters, an iterative scheme was employed.
 298 A custom coefficient of agreement (C_a) was used to enable Boolean comparison between
 299 iterations. All mooring instruments in the top 25 m were used for the calibration. For
 300 the temperature calibration, the model output was compared to the linearly interpolated
 301 data at every grid node and the root mean squared error ($RMSE_{\Theta,model}$) was computed
 302 and then normalized by the standard deviation of daily averaged and linearly interpo-
 303 lated mooring data ($STD_{\Theta,mooring}$). For the salinity data, the model output was linearly
 304 interpolated to the precise depth of each salinity instrument, then the root mean squared
 305 error ($RMSE_{SA,model}$) was computed and normalized by the standard deviation of the
 306 salinity data ($STD_{SA,mooring}$). The temperature score ($\frac{RMSE_{\Theta,model}}{STD_{\Theta,mooring}}$) and the salinity
 307 score ($\frac{RMSE_{SA,model}}{STD_{SA,mooring}}$) were weighted to take into account the number of temperature
 308 measurements (n_T) and conductivity measurements (n_C). For example, if there were 10
 309 temperature data points and four conductivity data points on the mooring line, the tem-
 310 perature score was weighted by $10/(10+4)$ and the salinity score was weighted by $4/(10+4)$.

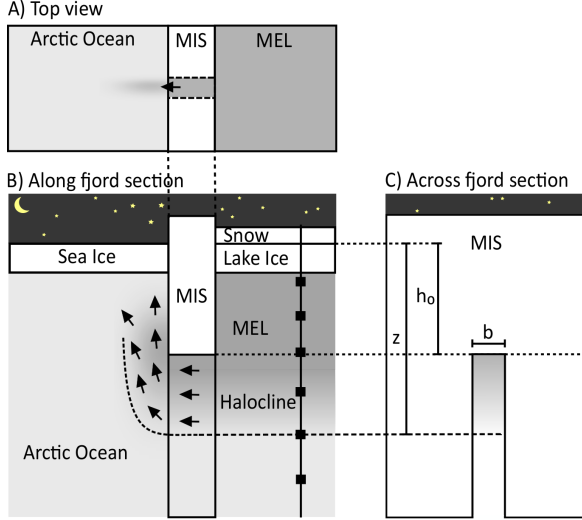


Figure 4. Schematic of the outflow of the lake through the basal channel of the ice shelf. A modified weir equation using a two layer simplification (equation 3) is used to constrain the number of parameters related to the outflow. A) Top view. B) Along fjord section. C) Across fjord section through MIS. Note: not to scale

311 To summarize, the C_a was computed with the following equation:

$$C_a = \left(\frac{n_T}{n_T + n_c} \left(\frac{RMSE_{\Theta, model}}{STD_{\Theta, mooring}} \right) + \frac{n_c}{n_T + n_c} \left(\frac{RMSE_{SA, model}}{STD_{SA, mooring}} \right) \right)^{-1} \quad (4)$$

312 The normalization by the standard deviation of the mooring data allowed combination
 313 of temperature and salinity data by placing them on a similar scale. The weights allowed
 314 combination of these evaluation scores by adjusting their importance according to the re-
 315 spective number of measurements. The -1 exponent was used to yield a positive rela-
 316 tionship between C_a and the model skill (i.e. a high C_a means a good agreement). A value
 317 around 1 would indicate that the model performed poorly, since the $RMSE$ would have
 318 the same magnitude as the STD (basically random). On the other hand, a value of 10
 319 would mean the model was very skillful since the $RMSE$ would be 10 times smaller than
 320 the STD .

321 Figure 5 is a schematic of the iterative model calibration workflow. The first step
 322 was to write the boundary and initial conditions into the model mesh (1). Then, a pair
 323 of outflow coefficients ($C_e b$ and h_0) was selected in order to calculate the daily outflow
 324 throughout the winter (2). Next, the mixing coefficients returning the highest C_a were
 325 found for day 1 (3-6). Steps 4-6 were repeated for every consecutive day. Once the daily
 326 mixing coefficients were determined, the C_a for the whole winter was computed (7) and
 327 steps 2-7 were repeated, narrowing down on the optimal $C_e b / h_0$ pair. Finally, the pair
 328 of outflow coefficients returning the highest C_a for the whole winter was selected as the
 329 best fitting parameters. This procedure was repeated for the remaining seven winters
 330 of mooring data (2011-2019). The model version with the best fitting parameters for each
 331 winter was used to generate the output in the Results section.

332 4 Model Results and Validation

333 4.1 Temperature

334 Figure 6A shows the daily averaged and linearly interpolated mooring data. The
 335 annual cycle of deepening and shoaling of MEL is clearly visible, as is the sharp temper-

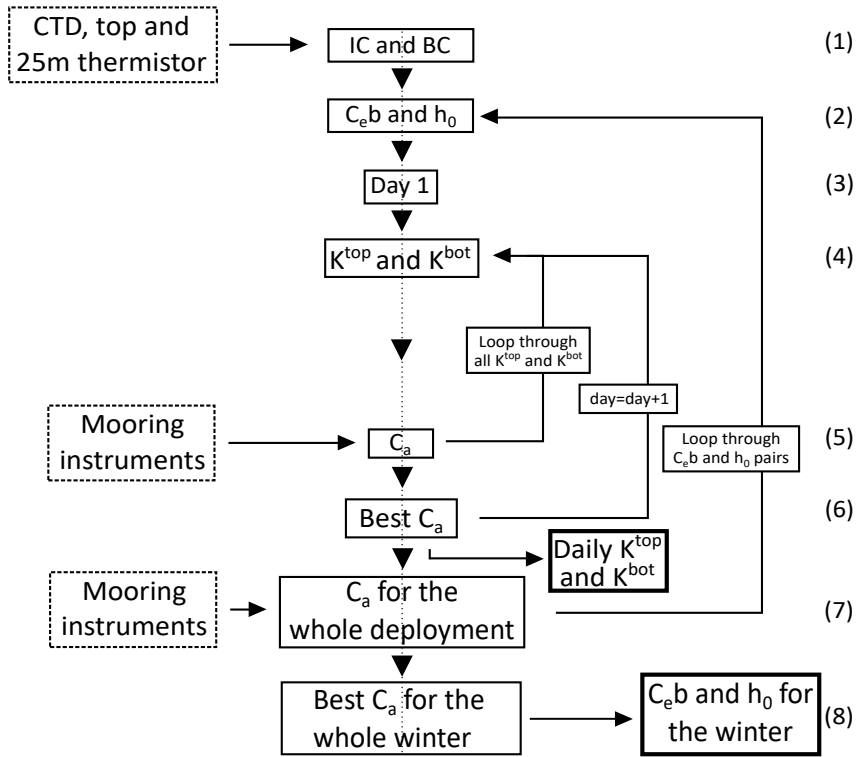


Figure 5. Once the initial conditions (IC) and the boundary conditions (BC) are implemented into the mesh, the model loops through the possible outflow coefficients ($C_e b$ and h_0) for every winter and through the possible mixing coefficients for every winter day. (See text for detailed explanation)

336 ature gradient is associated with the halocline. The maximum temperature in MEL is
 337 reached around mid-August and decreases until the following summer. The temperature
 338 of the water below the halocline is far less variable than the temperature above the halo-
 339 cline.

340 Temperature output from the model (Figure 6B) agrees well with the temperature
 341 data from the mooring (RMSE=0.19°C, STD=0.17°C, $r^2=0.97$, bias=0.067°C). Figure
 342 6C shows the difference between the model and the linearly interpolated mooring data.
 343 The model output appears as a smoothed version of the mooring data, which demon-
 344 strates that the main seasonal physical characteristics are reproduced. Three main dif-
 345 ferences can be observed between the model and the mooring data. First, the temper-
 346 ature oscillations (period around 10 days) above the halocline present in the mooring data
 347 are not reproduced in the model. Since there is no significant addition of heat from ver-
 348 tical processes during the winter, these oscillations must be the result of advection of hor-
 349 izontal temperature gradients, which are not considered in the model. The second ma-
 350 jor disparity is found near the halocline where slight deviations in the modeled halocline
 351 depth result in substantial temperature errors because of the sharp gradient at this lo-
 352 cation. This type of error is due to the simplified consideration of the outflow in the model,
 353 which is held constant for the whole winter. The last major difference is the inflow of
 354 cold water between 15 m and 22 m in the mooring data of 2015-2016 and 2016-2017 (Fig-
 355 ure 6A). This increased the error for the bottom part of the water column for many months.
 356 These main differences between the model and the mooring data are the result of the
 357 simplifications made in the model (one-dimension, no advection, rectangular weir out-
 358 flow). However, considering the visual and statistical agreement, the model is considered
 359 appropriate for the study of the full winter timeseries.

360 4.2 Salinity

361 The agreement between the model and the mooring salinity data is inferior to that
 362 for temperature, but the model still fits the main characteristics of the salinity profile
 363 in the fjord (Figure 7). The average RMSE is 2.0 g kg⁻¹, the standard deviation is 1.7
 364 g kg⁻¹ and the bias is 1.1 g kg⁻¹. The main discrepancies are found in the top of the wa-
 365 ter column where the model tends to diffuse more salt into the freshwater than the moor-
 366 ing instruments indicate. This is because the simulated halocline is compressed in the
 367 outflow process, increasing the salinity gradient to values higher than observed in situ.
 368 Since the salt flux is proportional to the gradient, more salt makes its way to the top layer
 369 as a result of this artifact. Nonetheless, the model shows the main features of the epishelf
 370 lake which are a freshwater layer atop a sharp halocline that moves upwards during the
 371 winter.

372 4.3 Outflow

373 The depth of the halocline (bottom of the epishelf lake) returned by the model is
 374 shown in Figure 8A, as well as the outflow parameters for each year (legend). The tra-
 375 jectories of the halocline from 2014 to 2019 are closely grouped but the first two years
 376 of the record (2011-2012 and 2012-2013) exhibit a more pronounced shoaling. The min-
 377 imum draft of the ice shelf (h_0) returned by the model is similar for every year (between
 378 6.7 and 7.9 m) except for the 2015-2016 year (5.3 m). The outflow friction-width coef-
 379 ficient ($C_e b$) varies more but stays within the range of realistic values. There are no per-
 380 ceptible trends in either $C_e b$ or h_0 .

381 Figure 8B shows the approximated flow rate through the channel according to the
 382 model (dashed lines) and the moored ADCP (solid lines). The total discharge of 2.0×10^8
 383 (2017-2018) and 2.3×10^8 m³ (2018-2019) for the model and 1.4×10^8 (2017-2018) and 0.9×10^8
 384 m³ (2018-2019) for the ADCP are similar.

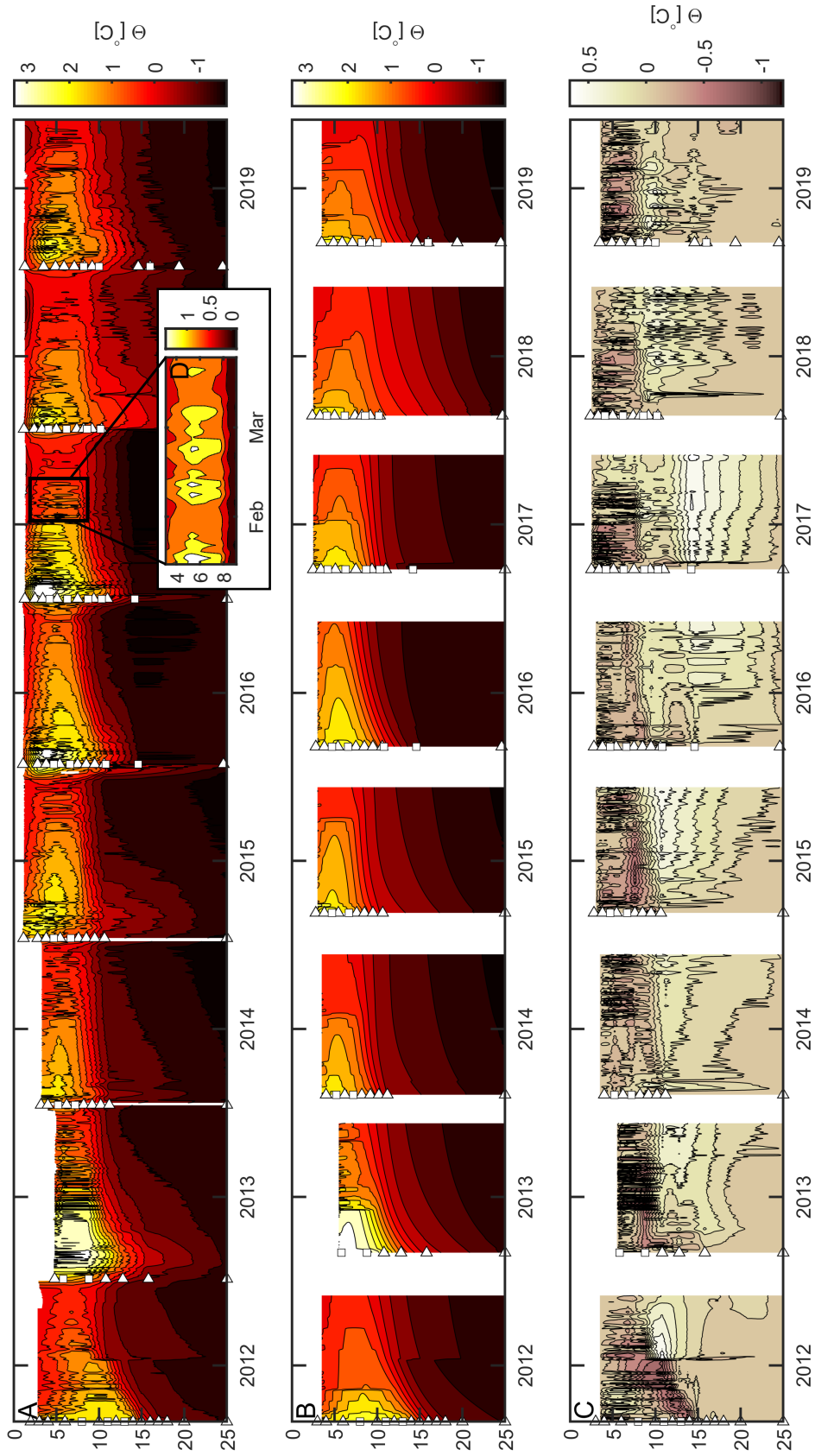


Figure 6. Temperature timeseries of the top of the water column in Milne Fiord. A) Temperature timeseries from the mooring (linearly interpolated). B) Temperature timeseries from the model. C) Difference between the model and the mooring data, positive values mean the model temperature is higher than the mooring temperature. Triangles show the location of the thermistors on the mooring line and the squares show the location of the conductivity instruments. D) Temperature oscillations close-up.

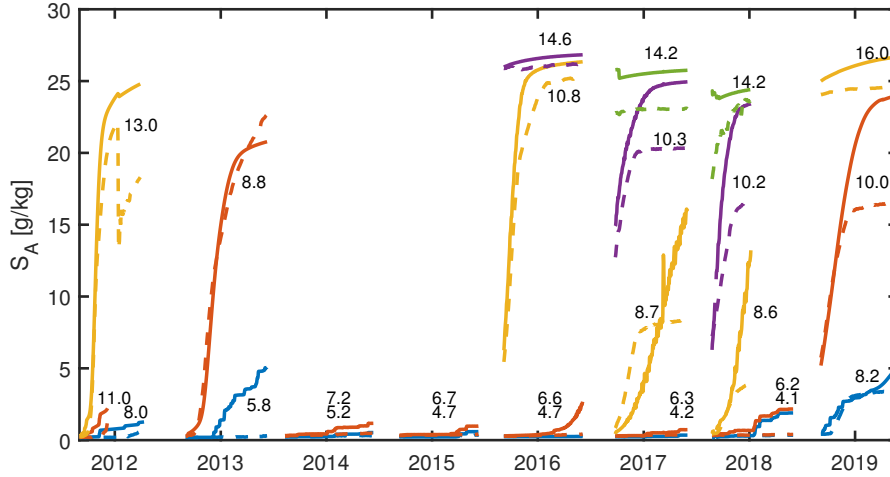


Figure 7. Salinity data from the model (solid line) at the depth of the conductivity instruments on the mooring (dashed line). Labels are the depth of the instruments, in meters.

4.4 Mixing

The daily mixing coefficients returned by the model are shown by the dots in Figure 9. The solid lines represent a 30 day moving average of apparent thermal diffusivity. The top layer of freshwater above the halocline experiences more mixing than the seawater below except during the first months (September and October) after the melt season. The total amount of mixing in the top of the water column differs greatly from year to year, with a minimum winter average of $2.5 \times 10^{-7} \text{ m}^2 \text{ s}^{-1}$ in 2015-2016 and maximum $1.2 \times 10^{-5} \text{ m}^2 \text{ s}^{-1}$ in 2018-2019. The mixing below the halocline is more uniform, spanning from $1.8 \times 10^{-7} \text{ m}^2 \text{ s}^{-1}$ in 2015-2016 to $2.3 \times 10^{-6} \text{ m}^2 \text{ s}^{-1}$ in 2013-2014.

If the model was over-mixing, the heat content of the freshwater layer would be lower in the model than in the mooring data, as a higher K_{Θ}^{top} implies a higher heat flux out of the top layer. Analysis of the heat content in the top freshwater layer shows that the model does not over- or under-mix, increasing the confidence in the results.

5 Discussion

5.1 Numerical Model

The one dimensional model employed in this study was shown to reproduce well the characteristics of the winter mooring data in Milne Fiord. It enables the description of the main physical mechanisms using only four different parameters. Consequently, these parameters can be examined in order to get a better understanding of Milne Fiord system. The iterative technique developed here could be used to investigate other systems that have mooring data.

5.2 Outflow

Outflow estimated from the ADCP data and the model agree well for 2018-2019, but there is significant divergence from late November 2017 to summer 2018. An event at the end of November 2017 resulted in a substantial increase in outflow velocity out of the fjord. Moreover, Figure 8B shows that the outflow remained higher following this outflow event, following the same trend as the model but with higher values. Unfortu-

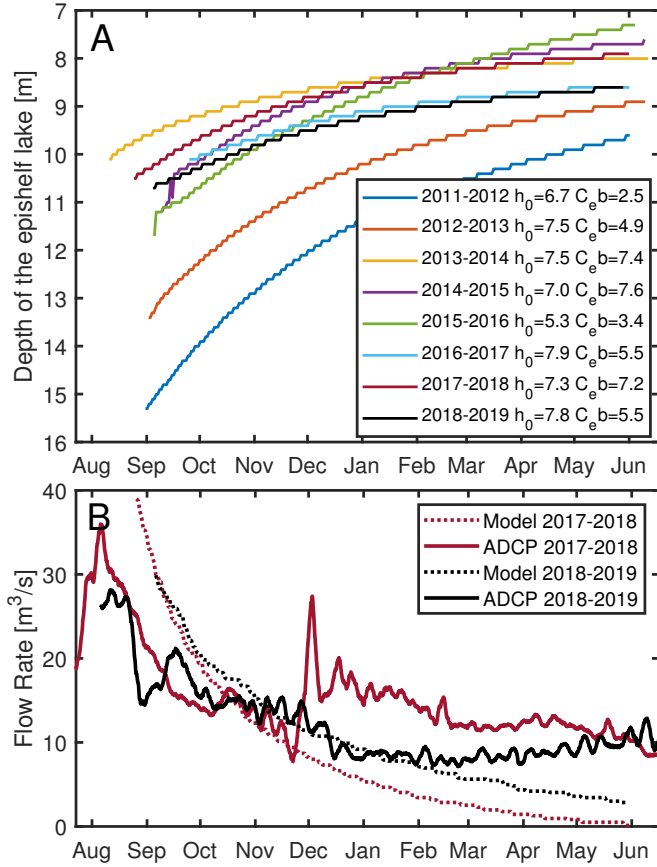


Figure 8. A) Depth of MEL (maximum N^2 value) given by the model for each winter. The staircase effect is due to the vertical discretization of the model (10 cm). Best fit outflow parameters h_0 and $C_e b$ for each winter are in the legend. B) Outflow through the basal channel in MIS. Dotted lines are the model estimation using the rectangular weir equation and an estimated lake area of 71.2 km^2 . Solid lines are the ADCP outflow estimation using a 10 day moving average.

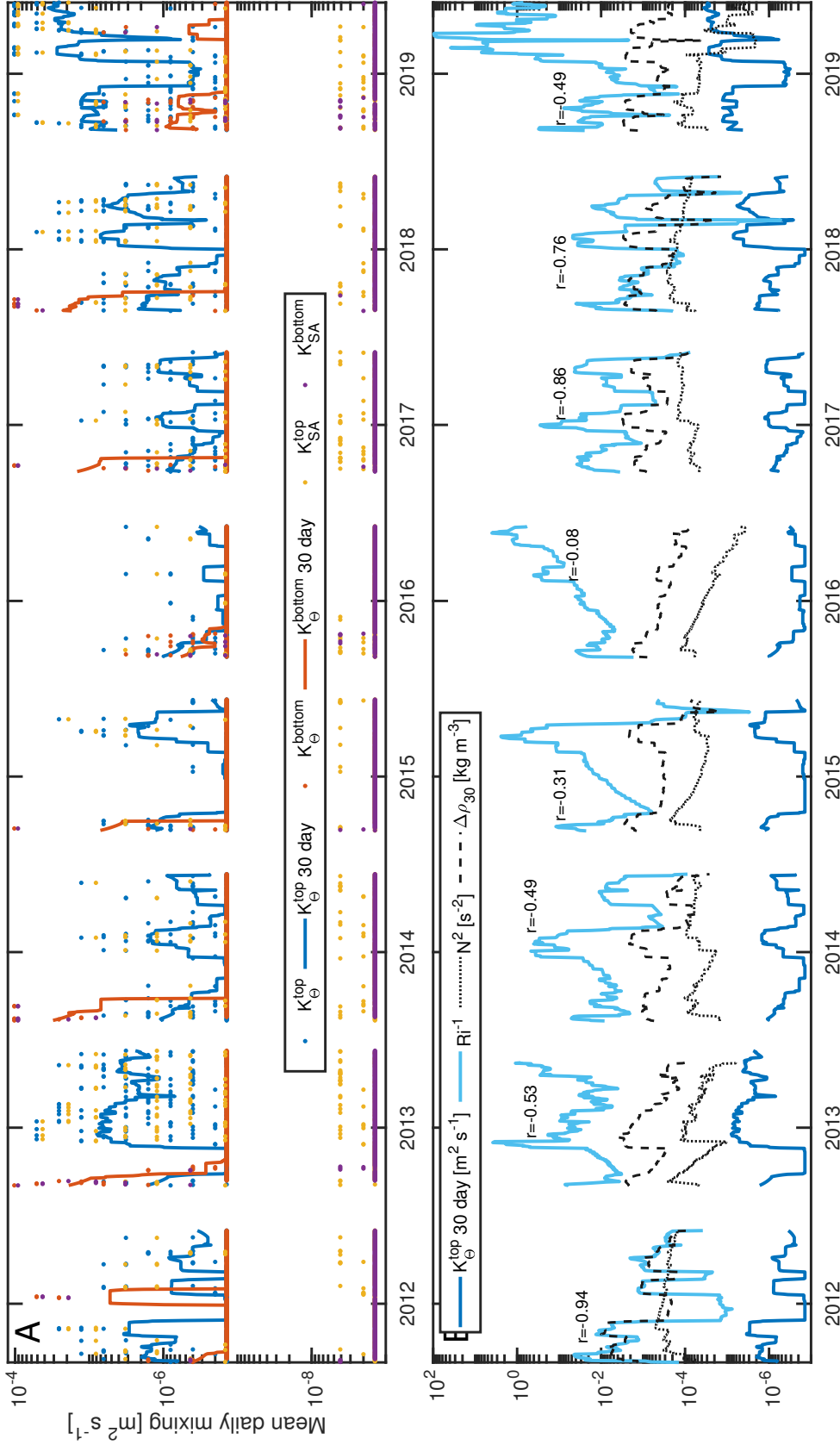


Figure 9. A) Daily mixing coefficients from the model, for the heat and salt transport equations for the top and bottom layers (dots). Solid lines are the 30 day averaged quantities for the top (blue) and bottom (red/orange) coefficients of the heat equation. Minimum possible values of daily mixing coefficients are the molecular diffusivities; $1.4 \times 10^{-7} \text{ m}^2 \text{ s}^{-1}$ for heat and $1.4 \times 10^{-9} \text{ m}^2 \text{ s}^{-1}$ for salt. B) 30 day averaged mixing coefficient (dark blue) and inverse of the Richardson number (light blue) computed according to equation 6. N^2 (dotted line) computed by the model and 30 day maximum density difference attributed to the temperature oscillations $\Delta\rho_{30}$ (dashed line) are used in equation 6. All values are for the top layer. Enhanced mixing (dark blue line) is linked to stronger eddy activity (dashed line) hence to a lower Richardson number (light blue line). The correlation coefficient (r) between Ri and mixing for each winter is above the Ri^{-1} line.

nately, it has not been possible to determine what caused this abrupt acceleration event captured by the ADCP. The ADCP flow rate in Figure 8B is estimated assuming the vertical velocity profile is constant across the cross section of the channel and assuming the channel cross section at the location of the ADCP did not change over time. These two assumptions are approximate, but this is the only way to compare in situ data with the model outflow. Considering its rough character, the comparison between the model results and the ADCP data is an order-of-magnitude type comparison. Since the trends are similar and the bulk outflow quantities match reasonably well; it is therefore concluded that they agree. Moreover, the model C_a is no worse in 2017-2019 than for the other years. This suggests the velocity increase, as experienced by the ADCP, is not directly linked to the epishelf lake.

The agreement between the model and the observations is not enough on itself to prove conclusively that the basal channel is the only outflow for the epishelf lake water. However, since the ADCP outflow is similar to the model and that ice penetrating radar measurements did not detect another probable path for outflow; it is reasonable to infer that the basal channel taken into account in this study is the main outflow path.

Channels under ice shelves and glacier tongues have attracted attention in recent years (e.g. Le Brocq et al., 2013; Alley et al., 2016; Dow et al., 2018). Buoyant water from subglacial melt and discharge converge in these longitudinal ice depressions, concentrating the melting in the channel apex (Millgate et al., 2013; Rignot & Steffen, 2008). Many recent studies estimated basal channel melt rates (Stanton et al., 2013; Dutrieux et al., 2013; Gourmelen et al., 2017; Alley et al., 2016), all agreeing that these locations experience enhanced melt (i.e. negative ice mass balance). For the present study, the outflow parameters of the model lead to the conclusion that the minimum draft of the ice shelf has not experienced a major change between September 2011 and July 2019. Indeed, if the melting was continuous in the channel, there would be a trend in the outflow coefficients. For example, h_0 would decrease year after year if the apex of the channel was continuously thinning, but this is not the case. The fact that h_0 went from 7.0 m (2014-2015) to 5.2 m (2015-2016) then up to 7.9 m (2016-2017) implies that the apex of the channel at the main constriction is in neutral mass balance over a multi-year time scale. Likewise, the fact that $C_e b$ does not show any particular trend also points towards a multi-year equilibrium in ice mass along the channel. This agrees with past evidence of ice accretion under Ward Hunt Ice Shelf (100 km to the east) (Jeffries et al., 1988). This result shows that the MIS basal channel is not necessarily an area of concentrated ice loss over a multi-year time scale. Although water at the apex of MIS channel is from a different source (epishelf lake) than the water at the apex of other ice shelf channels (buoyant plume from melting), this result is in marked contrast to what is found in the literature at other locations (Rignot & Steffen, 2008; Stanton et al., 2013; Dutrieux et al., 2013; Alley et al., 2016), but in agreement with Gladish et al. (2012) who show that basal channels may act to stabilize ice shelves. The calving of 45% of the MIS in July 2020 occurred along existing rifts but transverse to the channel (Figure 1). This suggests that the basal channel did not play a role in the break-up.

5.3 Mixing

Mixing during the first part of the winter (September-October) occurs both above and below the halocline. For the seawater layer, wind data from the Purple Valley weather station (2011 to present) and from a weather station on the ice shelf (2016-2018) shows that along-coast (NE) winds are low during the whole year except from July to September. If a shore lead is present or if the wind stress drives sea ice movement (Williams et al., 2006), coastal upwelling is expected to happen during these NE wind episodes. Examination of the 50 m thermistor shows a deflection of isotherms during these periods (not shown). It is then suggested that mixing occurring below the halocline just after the end of the melt season is linked to coastal upwelling, similar to R. H. Jackson et al. (2014). Other shelf processes (e.g. coastal trapped waves (Inall et al., 2015)) and fjord

processes (e.g. buoyancy driven circulation (Carroll et al., 2015)) possibly play a role below the epishelf lake. However, the focus here is on the epishelf lake. Aside from a peak in January 2012 and April 2019, mixing below the halocline is at molecular levels ($K_{\Theta}=1.4\times 10^{-7}\text{m}^2\text{s}^{-1}$) for the entire time after the residual summer mixing vanishes.

The mixing estimates given here are the first for an epishelf lake. There are very few quantitative estimates of mixing in ice-covered lakes, especially during winter when the effect of solar radiation is removed. Hence, the results presented here are particularly relevant to all low energy ice-covered water bodies at high latitude and mid-latitude lakes that experience substantial snow-cover. Although the average winter mixing coefficient for heat in MEL ($2.5\times 10^{-6}\text{m}^2\text{s}^{-1}$) is small relative to what is typical in lakes (e.g. Lin et al., 2020) or in the adjacent Arctic Ocean (e.g. Chanona et al., 2018), it is ~ 20 times larger than the rate of molecular diffusion. This means heat fluxes ~ 20 times higher, with an even greater impact on other tracers such as salinity or dissolved oxygen, as their molecular diffusion rate is lower.

Without wind or solar radiation, with minimal tides and an ice cover, the processes leading to mixing above the halocline are very limited in winter. Comparison of the temperature profile and salinity of the top layer ($\sim 0.2\text{g kg}^{-1}$) with studies on salt exclusion (Pieters & Lawrence, 2009; Bluteau et al., 2017) does not indicate this process could play an important role, especially over the entire winter. Moreover, in depth analysis of the meteorological data did not reveal correlation between mixing events and any of the available variables (temperature, wind, radiation, snow depth, atmospheric pressure). This demonstrates the isolating characteristic of the ice and snow cover.

On the other hand, examination of the water temperature timeseries shows that enhanced mixing is linked to the presence of 7 to 30 day oscillations in the temperature signal (Figure 6D). Because there is no addition of heat to the lake during winter, these temperature oscillations can only be due to advection of horizontal temperature gradients in MEL. Comparison of the temperature oscillations with internal waves seen in lakes and fjords did not yield any insights on their origin. However, the way heat appears and separates isotherms at $\sim 5\text{m}$ is reminiscent of horizontal eddies found in the Arctic Ocean (e.g. Hunkins, 1974; Timmermans et al., 2008) or in lakes (e.g. Kouraev et al., 2016; Forrest et al., 2013). Eddies are defined here as circular currents, in or close to geostrophic balance.

In order to link the temperature oscillations in the mooring data to possible eddies and to mixing, the thermal wind equation is used to calculate the vertical shear from the horizontal density gradient (Kundu et al., 2012) :

$$\frac{\partial u_1}{\partial x_3} = \frac{g}{\rho_0 f} \frac{\partial \rho}{\partial x_2} \quad (5)$$

Where f is the Coriolis frequency ($1.45\times 10^{-4}\text{s}^{-1}$ at 82.6°N). The thermal wind equation is then employed to scale the Richardson number:

$$Ri = \frac{N^2}{\left(\frac{\partial u_1}{\partial x_3}\right)^2} \approx \frac{N^2}{\left(\frac{g}{\rho_0 f} \frac{\partial \rho}{\partial x_2}\right)^2} \approx \frac{N^2}{\left(\frac{g}{\rho_0 f} \frac{\Delta \rho_{30}}{R_L}\right)^2} = \left(\frac{N^2 \rho_0 H}{g \Delta \rho_{30} \pi}\right)^2 \quad (6)$$

Where the Rossby radius of deformation ($R_L = NH/f \sim 500\text{m}$) is used to scale the horizontal span of the eddies. N^2 is computed with the model results. The vertical height scale (H) is taken as the distance between the bottom of the ice cover and the point where N^2 becomes larger than 0.01s^{-2} . Finally, $\Delta \rho_{30}$ is the 30 day maximum density variation related to the temperature oscillations. It is calculated using the mooring temperature data, assuming that the mooring captures the full range of the temperature anomalies (eddies) during a 30 day interval. The temperature oscillations (period of 7 to 30 days) from the mooring data have a greater amplitude than the 30 day temperature difference given by the model (i.e. $\Delta T_{30}^{\text{mooring}} > \Delta T_{30}^{\text{model}}$) which gives confidence that $\Delta \rho_{30}$ is attributable to horizontal movements (i.e eddies moving around). This is because there is no addition of heat in the epishelf lake, hence, a temperature increase seen by the mooring is a consequence of advection. Moreover, it is acknowledged that the model has higher

515 mixing coefficients when it encounters temperature oscillations because of the fitting method
 516 employed. However, consistently high mixing coefficients (30 day average) are undeni-
 517 ably related to increased vertical mixing.

518 Figure 9B shows the average Richardson number in the epishelf lake as well as the
 519 vertically averaged quantities used for its calculation (N^2 and $\Delta\rho_{30}$) and the 30 day av-
 520 eraged mixing coefficient for heat in the top layer returned by the model (K_{Θ}^{top}). Peaks
 521 in $\Delta\rho_{30}$ are definitely correlated with increased mixing. Simple linear correlation between
 522 $\log_{10}(\Delta\rho_{30})$ and $\log_{10}(K_{\Theta}^{top})$ gives a correlation coefficient (r) of 0.49 with a p-value \ll
 523 10^{-5} . This means that mixing is higher when the temperature oscillations (advection)
 524 are present. Figure 9B also shows that peaks in the inverse Richardson number (Ri^{-1})
 525 and mixing in the epishelf lake (K_{Θ}^{top}) are correlated. r is -0.43 and the p-value $\ll 10^{-5}$
 526 between $\log_{10}(Ri)$ and $\log_{10}(K_{\Theta}^{top})$ for the eight winters. The r value for each winter is
 527 in Figure 9B. Considering the thermal wind equation and the Rossby radius were used
 528 to scale Ri , correlation between the Ri and K_{Θ}^{top} means the phenomena linking mixing
 529 to the temperature oscillations is geostrophic by nature.

530 Similar results were obtained in the Arctic Ocean, where eddies in geostrophic bal-
 531 ance were found to increase vertical diffusivity by about one order of magnitude (Pnyushkov
 532 et al., 2018). Equation 6 can also be used to estimate horizontal velocities of around 1
 533 cm s^{-1} . This is similar to that reported in ice-covered lakes (Forrest et al., 2013; Bengts-
 534 son, 1996; Huttula et al., 2010) and what an ADCP measured in MEL in May 2011 (Hamilton,
 535 2016).

536 As previously mentioned, sources of energy in the epishelf lake are very limited dur-
 537 ing winter. Because mixing does not show any tendency to decrease after the end of the
 538 melt season, something has to be energizing the lake motion throughout the winter. Es-
 539 timation of the Ekman spin down time $t_E = D/(\sqrt{2Kf})$ (Pedlosky, 2013) with the height
 540 of the eddies $D \approx 8$ m and the eddy viscosity $K \approx 10^{-6} \text{ m}^2 \text{ s}^{-1}$, gives a time scale around
 541 5 days. This is obviously too short to attribute the existence of the eddies to residual
 542 energy from summer processes. The tidal amplitudes in Milne Fiord are very small (~ 10
 543 cm) and no tidal signal can be seen in the top thermistors. It is then quite unlikely that
 544 tides have an impact on the epishelf lake. Looking at other ice-covered lakes, numeri-
 545 cal modeling of Lake Untersee (Antarctica) has shown that the presence of an ice wall
 546 created a gyre in winter due to the change of water properties following ice-water inter-
 547 actions (Steel et al., 2015). Since the main body of MEL is bordered by ice upfjord and
 548 downfjord (Figure 1), cooling of epishelf lake water due to ice melting could possibly lead
 549 to density gradients large enough to drive circulation and form eddies. This would ex-
 550 plain the presence of the eddies (and enhanced mixing) throughout winter. Correspond-
 551 ingly, baroclinic instability is thought to be one of the main formation mechanism for
 552 eddies in the Arctic Ocean (Pnyushkov et al., 2018; Zhao et al., 2014).

553 6 Conclusion

554 Here we have used a one-dimensional model to analyze the winter mooring data
 555 of the top water column in Milne Fiord from 2011 to 2019. Three major results stand
 556 out from the analysis.

- 557 1. The model outflow rates, together with two years of ADCP data and ice penetrat-
 558 ing radar surveys, show that the main outflow path for the epishelf lake water is
 559 likely through a basal channel under the ice shelf. This can be exploited in hy-
 560 drological studies of Milne Fiord watershed.
- 561 2. The model outflow coefficients indicate that the basal channel area is in ice mass
 562 equilibrium over a multi-year time scale. This contradicts most studies of basal
 563 channels which state that these ice features are usually rapidly evolving (e.g. Gourme-
 564 len et al., 2017; Alley et al., 2016). Our results imply that basal channels are not
 565 necessarily linked to active destabilization, and that further investigation of ocean

566 properties within individual channels are required to better understand their time-
 567 evolving nature and potential role in ice shelf breakup.

568 3. The model mixing coefficients reveal that mixing is greater in the epishelf lake than
 569 in the seawater below the halocline. Enhanced mixing in the epishelf lake is linked
 570 to temperature oscillations with periods from 7 to 30 day. Moreover, estimation
 571 of the Richardson number suggests that enhanced mixing in the epishelf lake is
 572 linked to one or more geostrophic wave-like structures (eddies). This demonstrates
 573 that low energy physical processes can play a significant role in isolated settings
 574 such as epishelf lakes, but also other lakes and fjords experiencing a significant ice
 575 cover and limited external forcing.

576 Acknowledgments

577 The authors would like to express their gratitude to the following funding agencies: Nat-
 578 ural Sciences and Engineering Research Council of Canada (JB: CGSM-6563, BEL: NRS-
 579 2018-517975; RGPIN-2018-04843, DM: NRS-2011-402314; RGPIN-2016-06244), the Po-
 580 lar Continental Shelf Program (DM: 604-12; 626-13; 651-14; 642-15; 636-16; 647-17; 627-
 581 18; 651-19), les Fonds de Recherche Nature et Technologies du Qubec (JB: 270157), the
 582 Northern Scientific Training Program (JB), ArcticNet: GO-Ice: Glacier-Ocean-Iceberg
 583 Dynamics in a Changing Canadian Arctic, Impacts of the Changing Global Environment
 584 at Nunavuts Northern Frontier, Freshwater resources of the Eastern Canadian Arctic (DM,
 585 AKH, JB), Canada Foundation for Innovation (DM: 31410) and the Ontario Research
 586 Foundation (DM: 31410). We are also thankful for the logistical support given by the
 587 Polar Continental Shelf Program and we would like to thank all the individual who took
 588 part in field campaigns in Milne Fiord over the years. The data used in this study is pub-
 589 licly available through the Polar Data Catalogue (CCIN 12101 and 12102; <https://polardata.ca/>).

590 References

- 591 Aksenov, Y., Ivanov, V. V., Nurser, A. G., Bacon, S., Polyakov, I. V., Coward,
 592 A. C., . . . Beszczynska-Moeller, A. (2011). The Arctic circumpolar boundary
 593 current. *Journal of Geophysical Research: Oceans*, *116*(C9).
- 594 Alley, K. E., Scambos, T. A., Siegfried, M. R., & Fricker, H. A. (2016). Impacts of
 595 warm water on Antarctic ice shelf stability through basal channel formation.
 596 *Nature Geoscience*, *9*(4), 290–293.
- 597 Bengtsson, L. (1996). Mixing in ice-covered lakes. *Hydrobiologia*, *322*, 91–97.
- 598 Bennike, O., & Weidick, A. (2001). Late Quaternary history around Nioghalvfjords-
 599 fjorden and Jøkelbugten, North-East Greenland. *Boreas*, *30*(3), 205–227.
- 600 Bluteau, C. E., Pieters, R., & Lawrence, G. A. (2017). The effects of salt exclusion
 601 during ice formation on circulation in lakes. *Environmental Fluid Mechanics*,
 602 *17*(3), 579–590.
- 603 Carroll, D., Sutherland, D. A., Shroyer, E. L., Nash, J. D., Catania, G. A., &
 604 Stearns, L. A. (2015). Modeling turbulent subglacial meltwater plumes:
 605 Implications for fjord-scale buoyancy-driven circulation. *Journal of Physical*
 606 *Oceanography*, *45*(8), 2169–2185.
- 607 Chanona, M., Waterman, S., & Gratton, Y. (2018). Variability of internal wave-
 608 driven mixing and stratification in Canadian Arctic shelf and shelf-slope waters.
 609 *Journal of Geophysical Research: Oceans*, *123*(12), 9178–9195.
- 610 Dow, C. F., Lee, W. S., Greenbaum, J. S., Greene, C. A., Blankenship, D. D.,
 611 Poinar, K., . . . Zappa, C. J. (2018). Basal channels drive active surface
 612 hydrology and transverse ice shelf fracture. *Science Advances*, *4*(6), eaao7212.
- 613 Dutrieux, P., Vaughan, D. G., Corr, H. F., Jenkins, A., Holland, P. R., Joughin,
 614 I., & Fleming, A. (2013). Pine Island Glacier Ice Shelf melt distributed at
 615 kilometre scales. *The Cryosphere*, *7*, 1543–1555.
- 616 Forrest, A. L., Laval, B. E., Pieters, R., & SS Lim, D. (2013). A cyclonic gyre in an

- ice-covered lake. *Limnology and Oceanography*, 58(1), 363–375.
- 617 Gargett, A. E. (2003). Differential diffusion: An oceanographic primer. *Progress in*
618 *Oceanography*, 56(3-4), 559–570.
- 619 Gibson, J. A., & Andersen, D. T. (2002). Physical structure of epishelf lakes of the
620 southern Bunge Hills, East Antarctica. *Antarctic Science*, 14(3), 253–261.
- 621 Gladish, C. V., Holland, D. M., Holland, P. R., & Price, S. F. (2012). Ice-shelf basal
622 channels in a coupled ice/ocean model. *Journal of Glaciology*, 58(212), 1227–
623 1244.
- 624 Gourmelen, N., Goldberg, D. N., Snow, K., Henley, S. F., Bingham, R. G., Kimura,
625 S., . . . others (2017). Channelized melting drives thinning under a rapidly
626 melting Antarctic ice shelf. *Geophysical Research Letters*, 44(19), 9796–9804.
- 627 Hamilton, A. K. (2016). *Ice-ocean interactions in Milne Fiord* (PhD thesis). Univer-
628 sity of British Columbia.
- 629 Hamilton, A. K., Laval, B. E., Mueller, D., Vincent, W. F., & Copland, L. (2017).
630 Dynamic response of an Arctic epishelf lake to seasonal and long-term forcing:
631 implications for ice shelf thickness. *The Cryosphere*, 11(5), 2189–2211.
- 632 Hunkins, K. L. (1974). Subsurface eddies in the Arctic Ocean. In *Deep sea research*
633 *and oceanographic abstracts* (Vol. 21, pp. 1017–1033).
- 634 Huttula, T., Pulkkanen, M., Arkhipov, B., Leppäranta, M., Solbakov, V., Shira-
635 sawa, K., & Salonen, K. (2010). Modelling circulation in an ice-covered lake.
636 *Estonian Journal of Earth Sciences*, 59(4), 298.
- 637 Inall, M. E., Nilsen, F., Cottier, F. R., & Daae, R. (2015). Shelf/fjord exchange
638 driven by coastal-trapped waves in the arctic. *Journal of Geophysical Research:*
639 *Oceans*, 120(12), 8283–8303.
- 640 Jackson, J. M., Lique, C., Alkire, M., Steele, M., Lee, C. M., Smethie, W. M., &
641 Schlosser, P. (2014). On the waters upstream of Nares Strait, Arctic Ocean,
642 from 1991 to 2012. *Continental Shelf Research*, 73, 83–96.
- 643 Jackson, P. R., & Rehmann, C. R. (2014). Experiments on differential scalar mix-
644 ing in turbulence in a sheared, stratified flow. *Journal of Physical Oceanogra-*
645 *phy*, 44(10), 2661–2680.
- 646 Jackson, R. H., Lentz, S. J., & Straneo, F. (2018). The dynamics of shelf forcing in
647 greenlandic fjords. *Journal of Physical Oceanography*, 48(11), 2799–2827.
- 648 Jackson, R. H., Straneo, F., & Sutherland, D. A. (2014). Externally forced fluctu-
649 ations in ocean temperature at Greenland glaciers in non-summer months. *Nat-*
650 *ure Geoscience*, 7(7), 503–508.
- 651 Jeffries, M. O. (1985). *Physical, chemical and isotopic investigations of Ward Hunt*
652 *Ice Shelf and Milne Ice Shelf, Ellesmere Island, NWT* (PhD thesis). University
653 of Calgary.
- 654 Jeffries, M. O., Sackinger, W. M., Krouse, H. R., & Serson, H. V. (1988). Water
655 circulation and ice accretion beneath Ward Hunt Ice Shelf (northern Ellesmere
656 Island, Canada), deduced from salinity and isotope analysis of ice cores. *An-*
657 *nals of Glaciology*, 10, 68–72.
- 658 Kindsvater, C. E., & Carter, R. W. (1959). Discharge characteristics of rectangu-
659 lar thin-plate weirs. *Transactions of the American Society of Civil Engineers*,
660 124(1), 772–801.
- 661 Kirillin, G., Forrest, A., Graves, K., Fischer, A., Engelhardt, C., & Laval, B. (2015).
662 Axisymmetric circulation driven by marginal heating in ice-covered lakes. *Geo-*
663 *physical Research Letters*, 42(8), 2893–2900.
- 664 Kouraev, A. V., Zakharova, E. A., Rémy, F., Kostianoy, A. G., Shimaraev, M. N.,
665 Hall, N. M., & Suknev, A. Y. (2016). Giant ice rings on lakes Baikal and Hov-
666 sgol: Inventory, associated water structure and potential formation mechanism.
667 *Limnology and Oceanography*, 61(3), 1001–1014.
- 668 Kundu, P., Cohen, I., & Dowling, D. (2012). *Fluid mechanics*. Academic Press, New
669 York, NY.

- 671 Laybourn-Parry, J., & Wadham, J. L. (2014). *Antarctic lakes*. Oxford University
672 Press.
- 673 Le Brocq, A. M., Ross, N., Griggs, J. A., Bingham, R. G., Corr, H. F., Ferraccioli,
674 F., ... others (2013). Evidence from ice shelves for channelized meltwater flow
675 beneath the Antarctic Ice Sheet. *Nature Geoscience*, *6*(11), 945–948.
- 676 Lin, S., Boegman, L., & Rao, Y. (2020). Characterizing spatial and temporal distri-
677 butions of turbulent mixing and dissipation in lake erie. *Journal of Great Lakes*
678 *Research*.
- 679 McDougall, T. J., & Barker, P. M. (2011). *Getting started with TEOS-10 and the*
680 *Gibbs seawater (GSW) oceanographic toolbox. SCOR/IAPSO WG127* [type].
- 681 Millgate, T., Holland, P. R., Jenkins, A., & Johnson, H. L. (2013). The effect of
682 basal channels on oceanic ice-shelf melting. *Journal of Geophysical Research:*
683 *Oceans*, *118*(12), 6951–6964.
- 684 Mortimer, C. A., Copland, L., & Mueller, D. R. (2012). Volume and area changes of
685 the Milne Ice Shelf, Ellesmere Island, Nunavut, Canada, since 1950. *Journal of*
686 *Geophysical Research: Earth Surface*, *117*(F4).
- 687 Mortimer, C. A., Sharp, M., & Van Wychen, W. (2018). Influence of recent warming
688 and ice dynamics on glacier surface elevations in the Canadian High Arctic,
689 1995–2014. *Journal of Glaciology*, *64*(245), 450–464.
- 690 Mueller, D., Copland, L., & Jeffries, M. O. (2017). Changes in Canadian Arctic
691 ice shelf extent since 1906. In *Arctic ice shelves and ice islands* (pp. 109–148).
692 Springer.
- 693 Pedlosky, J. (2013). *Geophysical fluid dynamics*. Springer Science & Business Me-
694 dia.
- 695 Pieters, R., & Lawrence, G. A. (2009). Effect of salt exclusion from lake ice on sea-
696 sonal circulation. *Limnology and Oceanography*, *54*(2), 401–412.
- 697 Pnyushkov, A., Polyakov, I. V., Padman, L., & Nguyen, A. T. (2018). Structure and
698 dynamics of mesoscale eddies over the laptev sea continental slope in the arctic
699 ocean. *Ocean Science*, *14*(5).
- 700 Rajewicz, J. S. (2017). *Channelized epishelf lake drainage beneath the Milne Ice*
701 *Shelf, Ellesmere Island, Nunavut* (Unpublished master’s thesis). Carleton Uni-
702 versity.
- 703 Rignot, E., & Steffen, K. (2008). Channelized bottom melting and stability of float-
704 ing ice shelves. *Geophysical Research Letters*, *35*(2).
- 705 Rizk, W., Kirillin, G., & Leppäranta, M. (2014). Basin-scale circulation and heat
706 fluxes in ice-covered lakes. *Limnology and Oceanography*, *59*(2), 445–464.
- 707 Sciascia, R., Straneo, F., Cenedese, C., & Heimbach, P. (2013). Seasonal variability
708 of submarine melt rate and circulation in an East Greenland fjord. *Journal of*
709 *Geophysical Research: Oceans*, *118*(5), 2492–2506.
- 710 Stanton, T. P., Shaw, W., Truffer, M., Corr, H., Peters, L., Riverman, K., ... Anan-
711 dakrishnan, S. (2013). Channelized ice melting in the ocean boundary layer
712 beneath Pine Island Glacier, Antarctica. *Science*, *341*(6151), 1236–1239.
- 713 Steel, H., McKay, C., & Andersen, D. (2015). Modeling circulation and seasonal
714 fluctuations in perennially ice-covered and ice-walled Lake Untersee, Antarc-
715 tica. *Limnology and Oceanography*, *60*.
- 716 Straneo, F., & Cenedese, C. (2015). The dynamics of Greenland’s glacial fjords and
717 their role in climate. *Annual Review of Marine Science*, *7*, 89–112.
- 718 Straneo, F., Hamilton, G. S., Sutherland, D. A., Stearns, L. A., Davidson, F., Ham-
719 mill, M. O., ... Rosing-Asvid, A. (2010). Rapid circulation of warm subtropi-
720 cal waters in a major glacial fjord in East Greenland. *Nature Geoscience*, *3*(3),
721 182–186.
- 722 Timmermans, M.-L., Toole, J., Proshutinsky, A., Krishfield, R., & Plueddemann, A.
723 (2008). Eddies in the Canada Basin, Arctic Ocean, observed from ice-tethered
724 profilers. *Journal of Physical Oceanography*, *38*(1), 133–145.

- 725 Turner, J. S. (1968). The influence of molecular diffusivity on turbulent entrainment
726 across a density interface. *Journal of Fluid Mechanics*, *33*(4), 639–656.
- 727 Vincent, W., Gibson, J., & Jeffries, M. (2001). Ice-shelf collapse, climate change,
728 and habitat loss in the Canadian high Arctic. *Polar Record*, *37*(201), 133–142.
- 729 Washam, P., Nicholls, K. W., Münchow, A., & Padman, L. (2019). Summer surface
730 melt thins Petermann Gletscher Ice Shelf by enhancing channelized basal melt.
731 *Journal of Glaciology*, *65*(252), 662–674.
- 732 Williams, W. J., Carmack, E. C., Shimada, K., Melling, H., Aagaard, K., Macdon-
733 ald, R. W., & Ingram, R. G. (2006). Joint effects of wind and ice motion
734 in forcing upwelling in Mackenzie Trough, Beaufort Sea. *Continental Shelf*
735 *Research*, *26*(19), 2352–2366.
- 736 Zhao, M., Timmermans, M.-L., Cole, S., Krishfield, R., Proshutinsky, A., & Toole, J.
737 (2014). Characterizing the eddy field in the arctic ocean halocline. *Journal of*
738 *Geophysical Research: Oceans*, *119*(12), 8800–8817.

Figure_1.

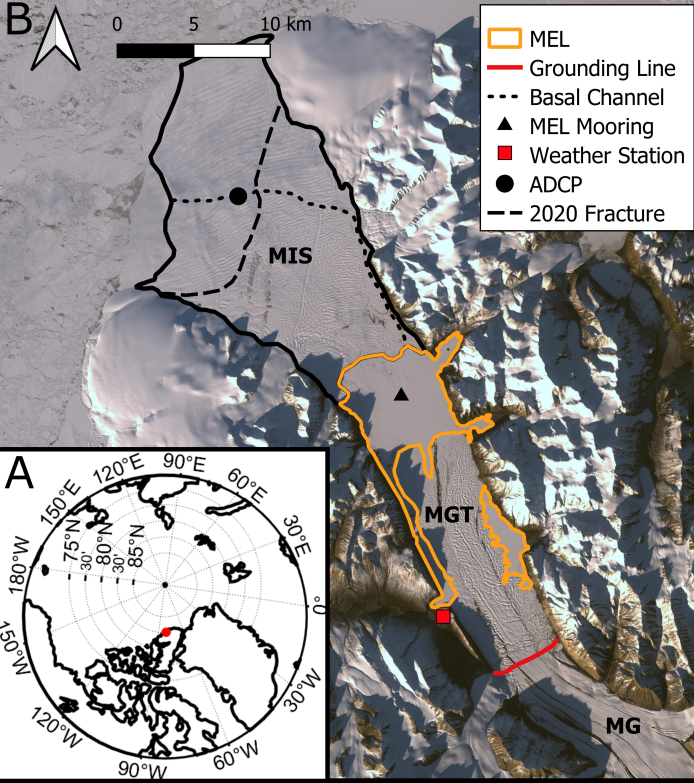


Figure_2.

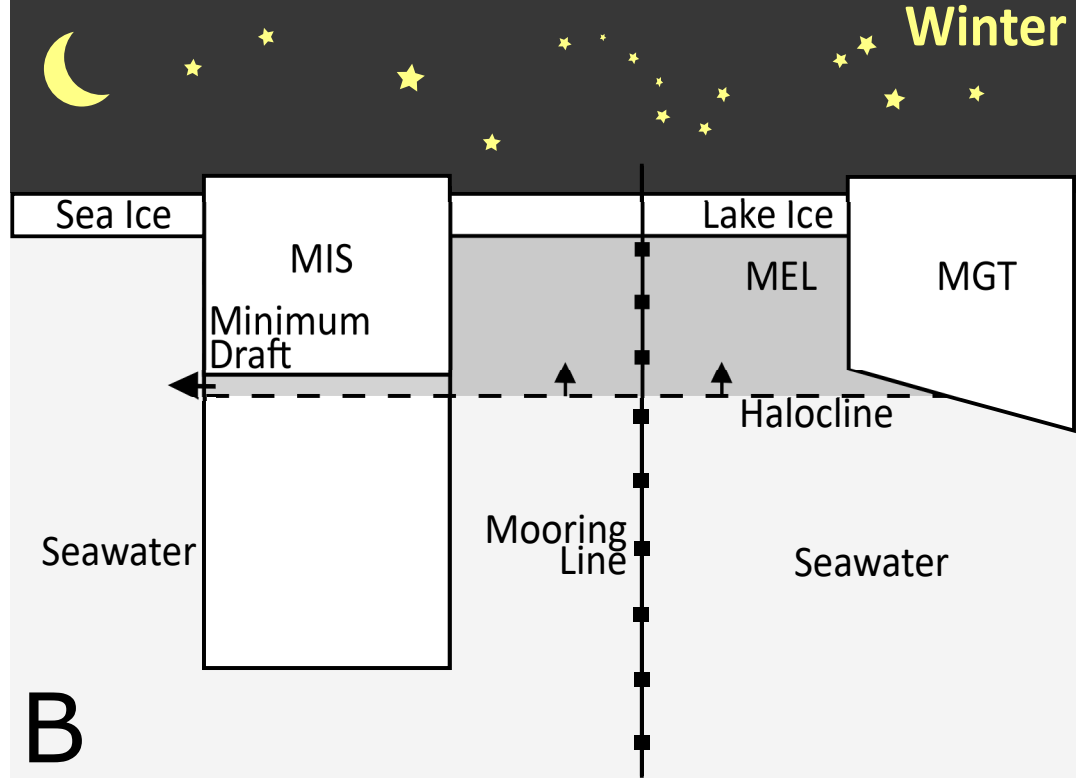
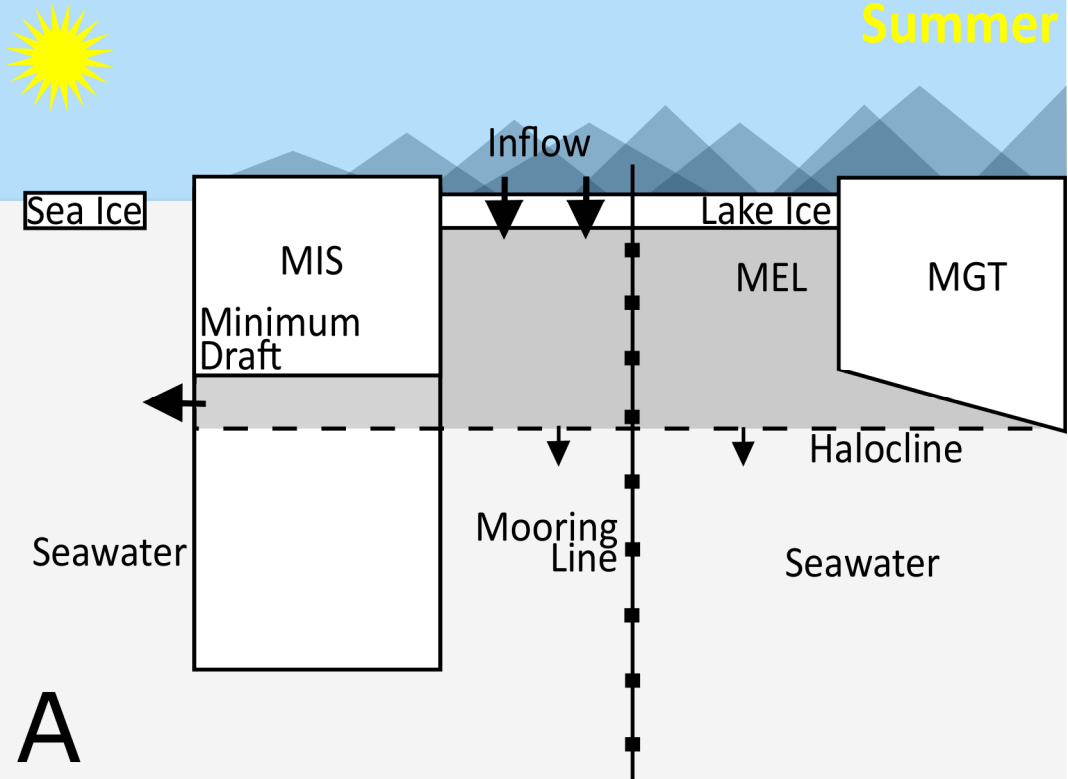


Figure_3.

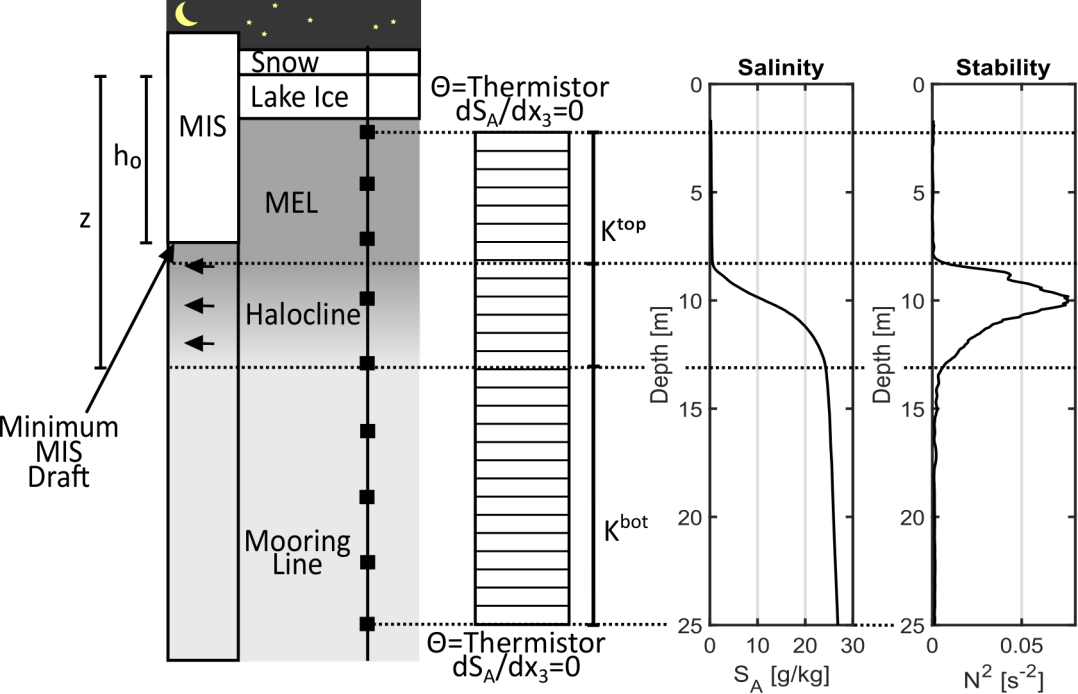
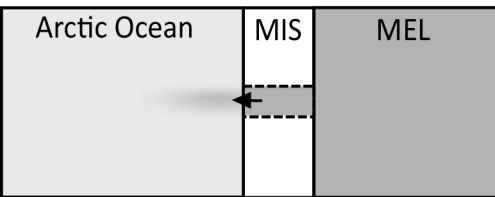
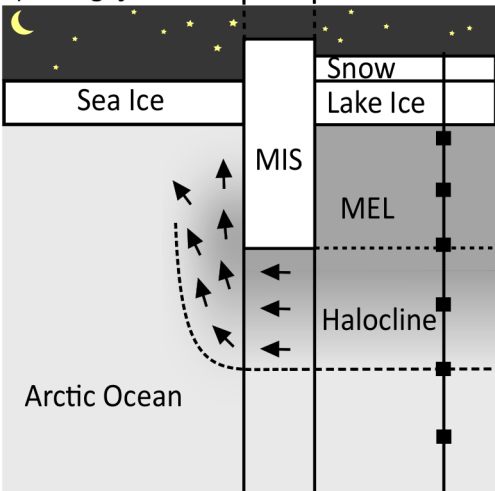


Figure_4.

A) Top view



B) Along fjord section



C) Across fjord section

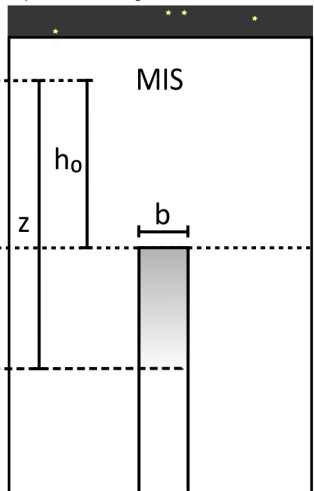


Figure_5.

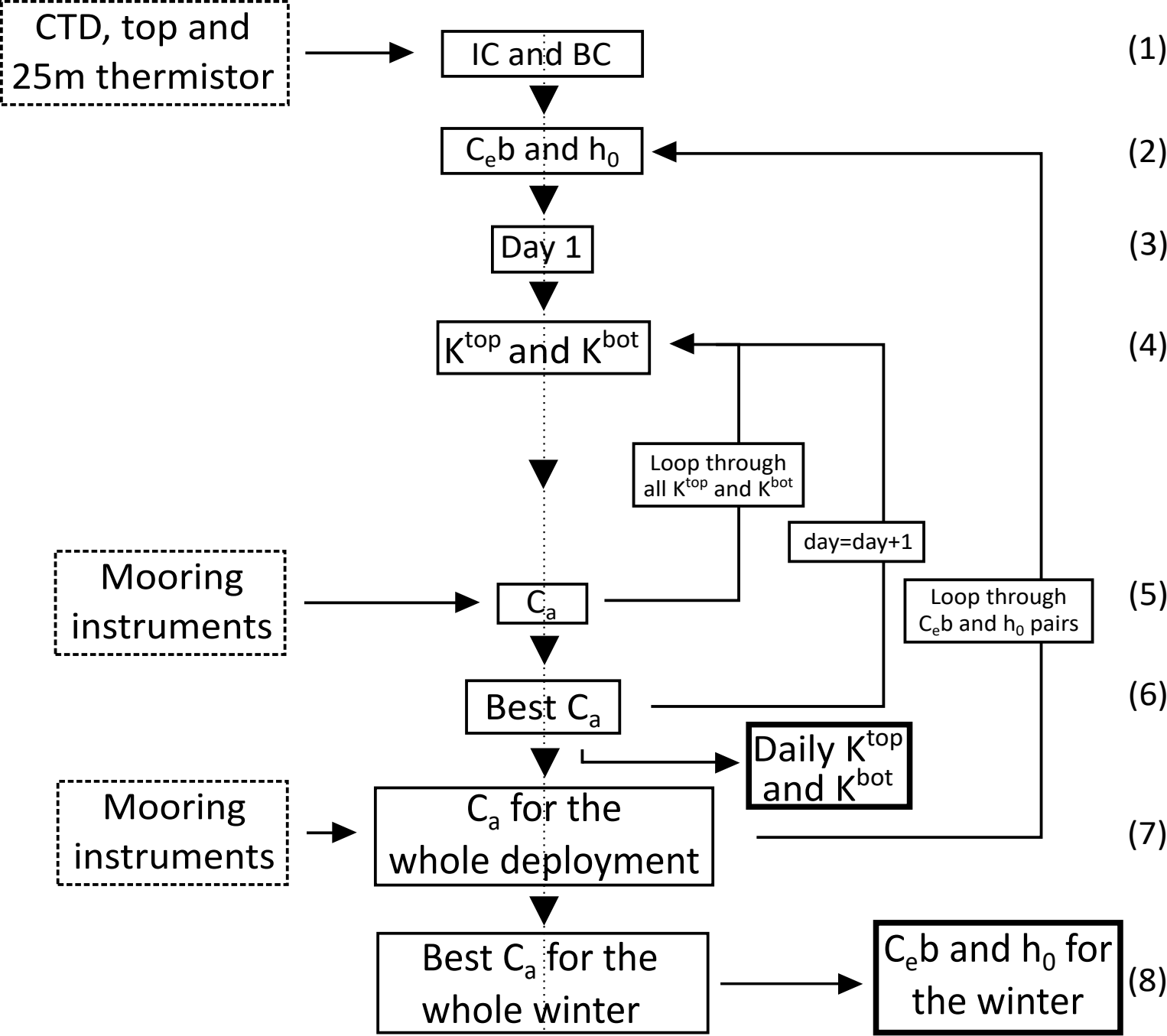


Figure_6.

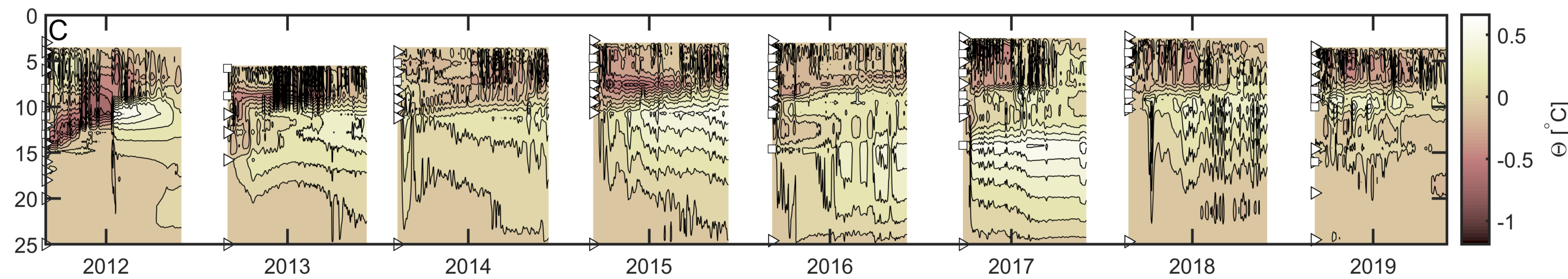
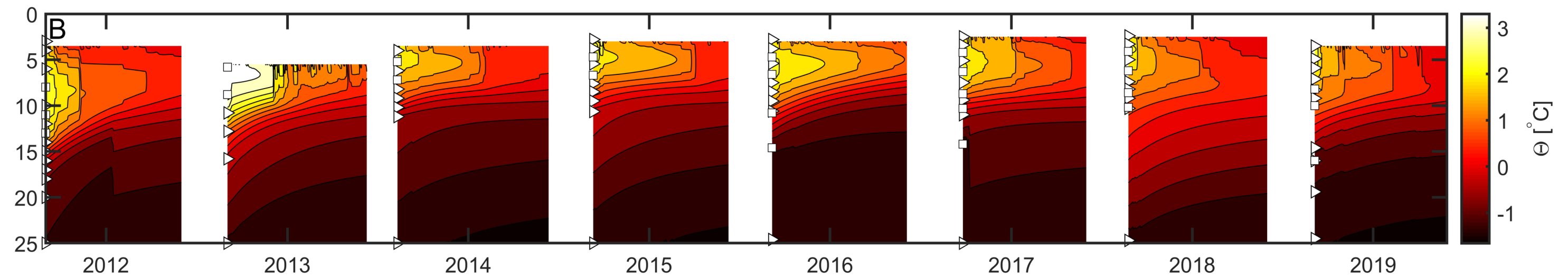
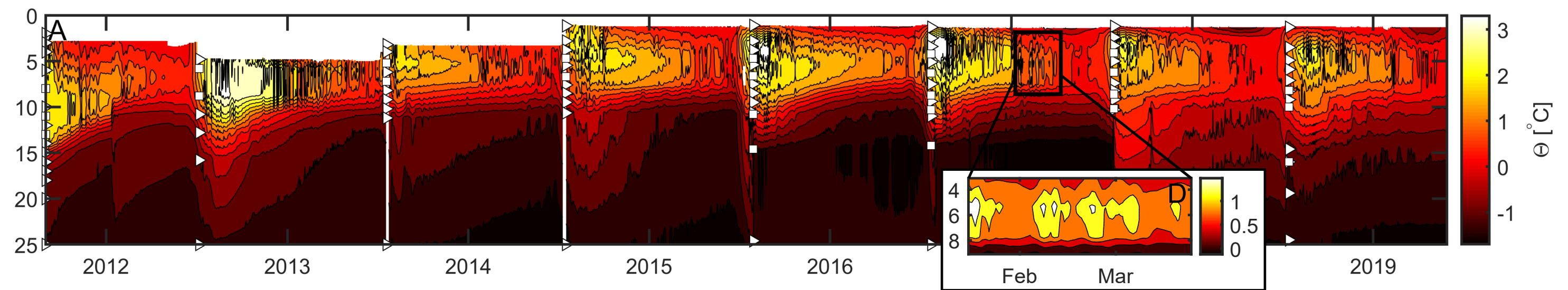


Figure_7.

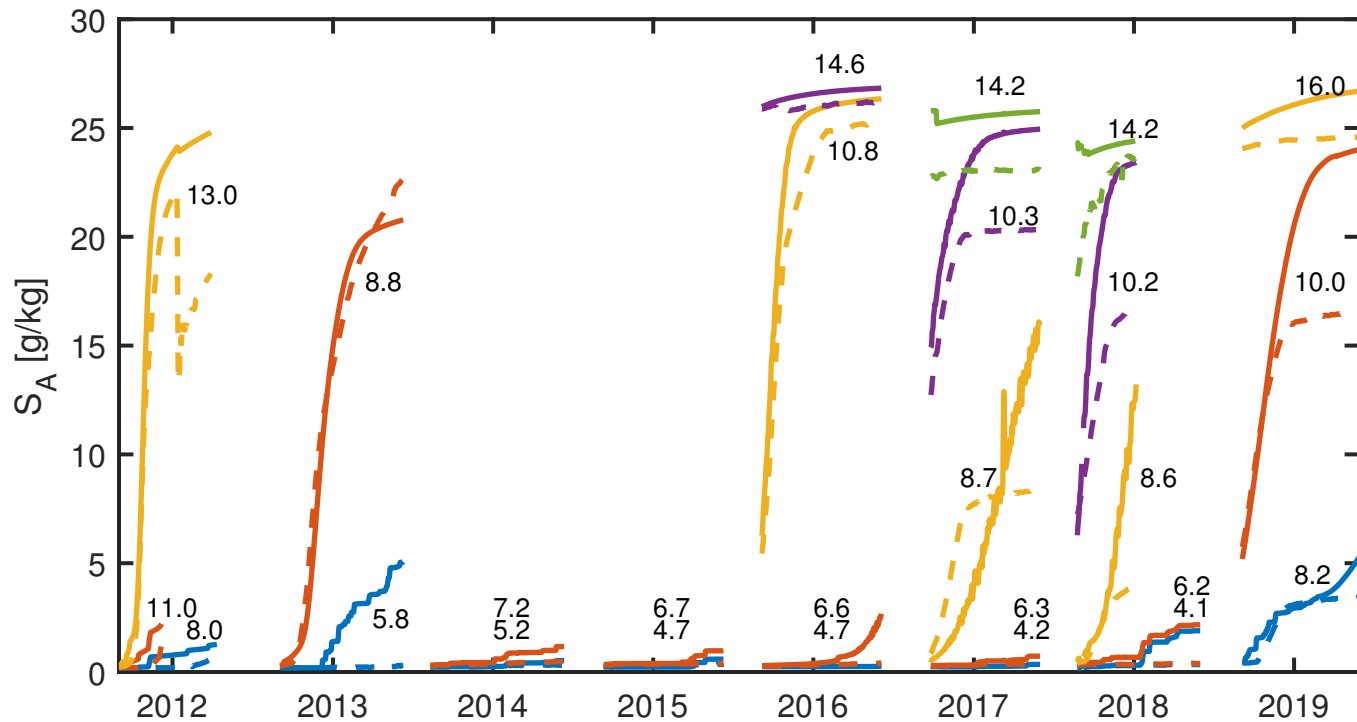


Figure_8.

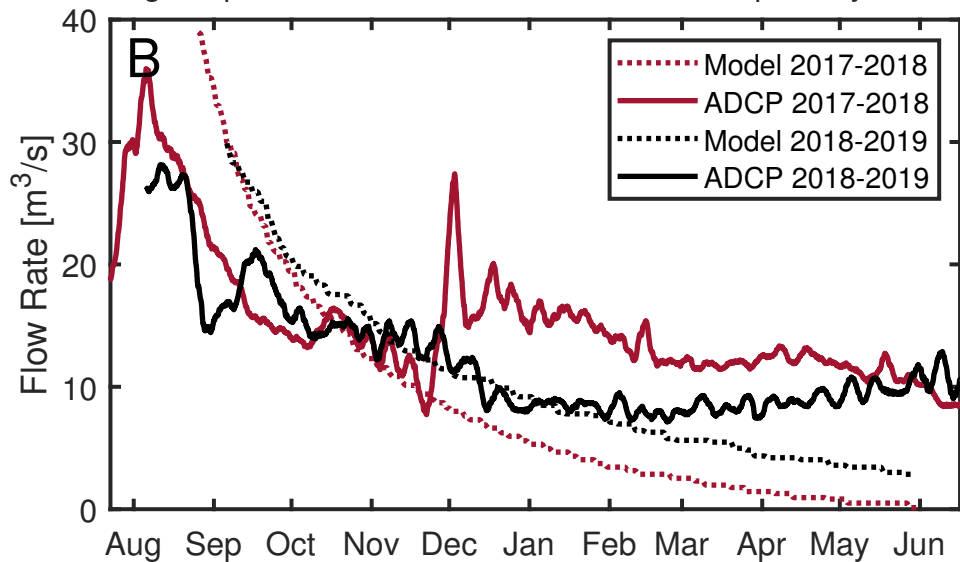
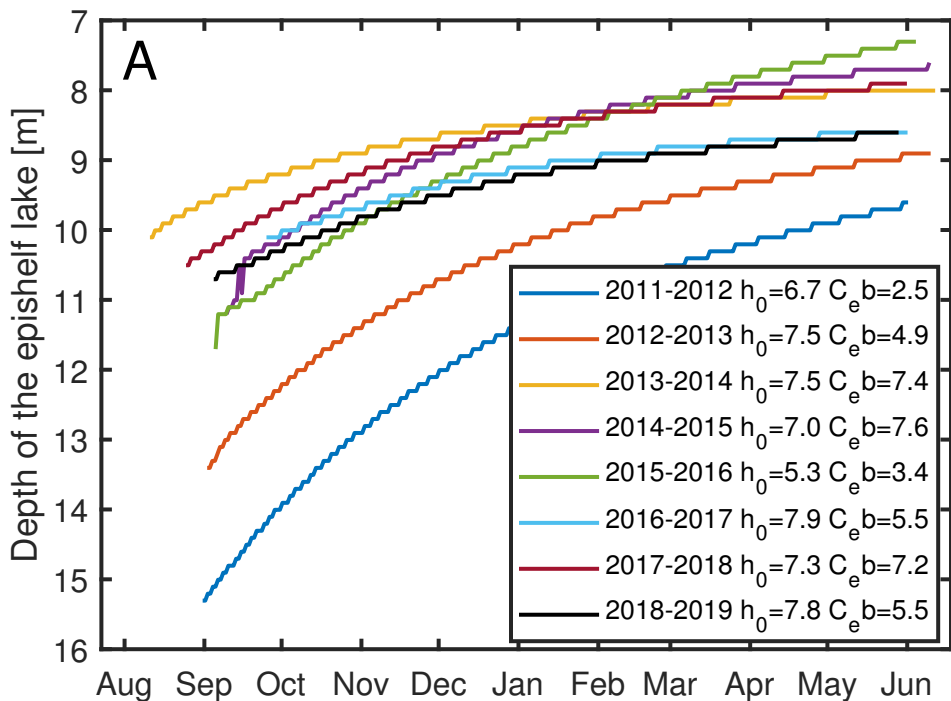


Figure_9.

